POLYOXOMETALATES

Open Access
REVIEW ARTICLE

Cluster-nuclei coassembled ultrathin materials: Recent progress and applications

Peilei He

School of Materials Science and Engineering, Tianjin University of Technology, Tianjin 300384, China

Cite This: *Polyoxometalates*, **2026**, *5*, 9140118

Read Online

ABSTRACT: The cluster-nuclei coassembly strategy, first reported by Wang et al. in 2019, refers to the coassembly of polyoxometalate (POM) clusters and inorganic nuclei affording ultrathin/subnanometer (sub-1 nm) materials such as nanowires, nanobelts, nanosheets, and nanotubes. These materials exhibit unique properties and hold promises for applications in catalysis, energy storage, photothermal conversion, and tumor treatment. This review discusses progress in cluster-nuclei coassembled ultrathin materials and covers their synthesis methods, well-defined structures, and application prospects, aiming to provide a roadmap for the future design and further development of sub-1 nm POM-nuclei coassembly systems.

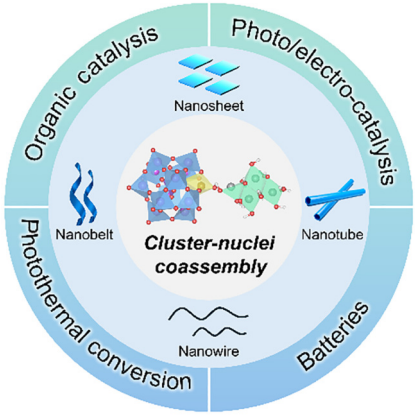

KEYWORDS: polyoxometalate, cluster-nuclei co-assembly, ultrathin, catalysis, subnanometer

1 Introduction

The dawn of nanotechnology dates back to the discovery of quantum confinement effects in the 1980s [1]. Brus was the first to explain how the size of semiconductor nanocrystals, known as quantum dots, determines their optoelectronic properties [2, 3]. Later, Bawendi et al. (1993) developed a high-precision high-temperature process enabling the large-scale production of high-quality optically tunable quantum dots [4]. This innovation paved the way for the commercialization of nanocrystals, which were initially applied in bioimaging and labeling and continue to drive exploration in cutting-edge fields such as photovoltaics, sensors, and quantum computing [5–8].

The three decades of 1980–2010 witnessed the rapid advancement of nanoscience driven by distinct properties emerging at the nanoscale [9]. However, confining the dimensions of nanoparticles to the ultrathin/subnanometer (sub-1 nm) scale remains difficult [10–13]. To address this challenge, Wang et al. developed a good solvent/poor solvent strategy and used it to construct various sub-1 nm materials [14, 15], including polymer-analogous [16, 17] and processable [18–20] GdOOH ultrathin nanowires with diameters of < 1 nm. Subsequently, other sub-1 nm nanostructures were reported, such as ultrathin molybdenum oxide nanorings [21], ultrathin tungsten bronze nanowires [22], hydroxyapatite sub-1 nm nanowires [23], and tungsten oxide sub-1 nm nanowires [24]. Recently, Wang et al. have developed a facile room-temperature synthesis of alkaline earth cation-bridged polyoxometalate (POM) clusters and assembled them into sub-1 nm nanowires. These nanowires self-organize into three-dimensional networks capable of effectively trapping over 10 types of volatile organic liquids, achieving remarkable absorption efficiencies with much lower mass fraction of nanowires [25].

Along with the construction of numerous subnano structures, a universal synthesis method was established in 2019 [26]. Wang et al. [26, 27] conceived a cluster-nuclei coassembly strategy relying on POM clusters, which are metal-oxygen nanoclusters typically containing oxygen atom-linked early transition metals in high oxidation states [28–30]. These clusters are renowned for their molecular diversity, forming well-defined anionic structures with a broad range of sizes and shapes [31, 32]. Prior to the discovery of the cluster-nuclei coassembly strategy, researchers primarily focused on developing POM-based hybrid systems. Numerous POM assemblies have been reported, such as honeycomb nanostructures [33], vesicles [34], fullerene-like spheres [35], and superlattice structures [36]. Consequently, POMs have found widespread applications in areas such as catalysis and materials science [37, 38]. Typically, the dimensions of Keggin- and Anderson-type POMs are below 1 nm. Therefore, the cluster-nuclei coassembly approach utilizes the fixed size of POM clusters as a built-in ruler to confine and dictate the dimensions of the assembled structures.

The growth mechanism of cluster-nuclei coassembly is

Received: November 29, 2025; **Revised:** January 5, 2026
Accepted: January 18, 2026

Address correspondence to hepeilei@email.tjut.edu.cn

https://doi.org/10.26599/POM.2026.9140118

fundamentally different from the classical LaMer mechanism followed by traditional nanoparticle growth. The LaMer mechanism, proposed by LaMer et al. in 1950, explains the formation of monodisperse nanoparticles by separating nucleation and growth [39, 40] and starts with a rapid nucleation burst as the monomer concentration surpasses the critical supersaturation concentration [41]. In the following controlled-growth phase, monomers diffuse onto existing nuclei without new nucleation, which results in a uniform particle size [42]. Building on this principle, the mechanism proposed for cluster-nuclei coassembly involves initial interactions between monomers and POM clusters during nucleation [26]. The increasing monomer concentration drives the formation of inorganic nuclei and their coassembly with POM clusters into primary building blocks, which subsequently self-organize via weak intermolecular forces. This process leads to diverse architectures and ultimately affords stable sub-1-nm materials. Wang et al. prepared a series of sub-1 nm materials through the coassembly of POM clusters with inorganic nuclei composed of, e.g., metal oxides (MO_x), high-entropy metal oxides (HEOs), metal sulfides (MS_x), metal hydroxides (MOH_x), and noble metals (NMs) [43]. These sub-1 nm materials demonstrated polymer-like properties and potential applications in catalysis, energy storage, photothermal conversion, and even tumor treatment [10]. The rapid advancement of characterization techniques has markedly accelerated exploration at the subnanometer scale. Aberration-corrected electron microscopy enables the in-depth characterization of materials at this scale, while cryo-electron microscopy allows the direct observation of individual POM clusters within subnano materials [14, 44]. Additionally, matrix-assisted laser desorption/ionization time-of-flight mass spectrometry (MALDI-TOF-MS) has confirmed the presence of POM clusters in cluster-nuclei coassemblies [45].

This review systematically outlines the latest advances in cluster-nuclei coassembled materials, focusing on the corresponding synthetic strategies, structural features, and functional applications. Section 3 elaborates on the synthesis and architecture of various hybrid systems, including MO_x-POM, HEO-POM, MOH_x-POM, MS_x-POM, and NM-POM ones, while Section 4 highlights their emerging applications, such as photo/electrocatalysis, catalytic organic reactions, batteries, solar steam generation, and seawater desalination. The review concludes with a perspective on the current challenges and future research directions of cluster-nuclei coassembly.

2 Mechanism of cluster-nuclei coassembly

The LaMer model was introduced in 1950 by LaMer et al. and is foundational for the nucleation and growth of colloidal nanoparticles [39]. Wang et al. (2019) found that POM cluster introduction can induce the formation of sub-1 nm structures (Fig. 1(a)), which represents a deviation from the classical LaMer model (Fig. 1(b)) [26]. To explain the growth of these structures, Wang et al. proposed the cluster-nuclei coassembly strategy. Figure 1(c)(i) depicts the cluster-nuclei coassembly pathway, whereas Fig. 1(c)(ii) shows the ligand-mediated shape-control pathway adhering to the classical LaMer model. In both cases, nuclei are formed during the initial nucleation stage. In the cluster-nuclei coassembly pathway, monomers and POM clusters interact during nucleation, and the monomer concentration simultaneously increases. These factors trigger the coassembly of nuclei and clusters into primary building blocks, which undergo further self-organization via weak interactions to form diverse structures, ultimately growing into sub-1 nm materials. Molecular dynamics (MD) simulations revealed that cluster-nuclei coassembly is mainly driven by Coulomb and van der Waals interactions [46] and can be attributed to energy minimization, as indicated by the reduction in the energies of Coulomb and van der Waals interaction between POMs and nuclei.

For the NiS_x-NiO_x-POM system as an example, NiS_x-NiO_x monomers initially interact with POM clusters. As the monomer concentration increases, NiS_x-NiO_x nuclei begin to form and subsequently coassemble with POM clusters to afford the NiS_x-NiO_x-POM product (Fig. 1(d)). In contrast, fullerene-like NiS_x-NiO_x hollow nanospheres are formed in the absence of POMs, as evidenced by transmission electron microscopy (TEM; inset of Fig. 1(d)). This structure-directing role of POMs was further demonstrated using NiCo hydroxide nuclei. In this case, a superlattice of sub-1 nm nanosheets (SNSs) (Fig. 1(e)) and spiral nanosheets (inset of Fig. 1(e)) were formed in the presence and absence of POMs, respectively.

Based on the mechanistic principles established for the current system, the direct substitution of POMs with typical noble metal clusters (e.g., Au, Ag, and Pd) may be challenging, the primary obstacle being electrostatic compatibility. The anionic POM clusters possess a high negative charge density, which is crucial for their strong electrostatic interaction with the positively charged ligands to drive the coassembly process. Moreover, the surface oxygen chemistry of POM clusters plays a critical role in their interaction with the inorganic nuclei [46]. In contrast, most ligand-protected NM clusters are either neutral or singly negatively charged, which results in a notably weaker electrostatic driving force and makes participation in cluster-nuclei coassembly unlikely.

Cluster-nuclei coassembly has been used to prepare diverse ultrathin nanomaterials, which are discussed in the following section.

3 Syntheses and structures of cluster-nuclei coassembled ultrathin materials

Sub-1 nm materials synthesized by combining POM clusters with inorganic nuclei include MO_x-POM (MO_x = CoO, ZnO, CuO, ZrO_2, TiO_2, MoO_3, MnO, Fe_3O_4, Y_2O_3, Yb_2O_3, CeO_2, Bi_2O_3, and NiO), HEO-POM, MOH_x-POM (MOH_x = $Ni(OH)_2$), MS_x-POM (MS_x = Cu_9S_5 and Ni_3S_2), and NM-POM systems and exhibit diverse architectures, such as nanowires, nanobelts, and nanosheets.

This section provides an overview of the compositions and structures of ultrathin nanomaterials formed via cluster-nuclei coassembly (Table 1), with most Keggin-type (e.g., PMo_{12}, PW_{12}, and $PMo_{11}Fe$) and Anderson-type (e.g., Mo_6 and W_6) POMs being suitable building blocks. Herein, we introduce cluster-nuclei coassembled ultrathin nanomaterials of six types (MO_x-POM, HEO-POM, MOH_x-POM, MS_x-POM, NM-POM, and other).

3.1 MO_x-POM

Conventional MO_x-POM ultrathin materials are foundational for understanding the cluster-nuclei coassembly mechanism. Owing to the similarity of POMs to metal oxides, the latter easily coassemble with the former. Hence, many kinds of metal oxides (e.g., CoO, ZrO_2, CuO, MoO_3, TiO_2, and ZnO) have been used to construct sub-1 nm MO_x-POM structures.

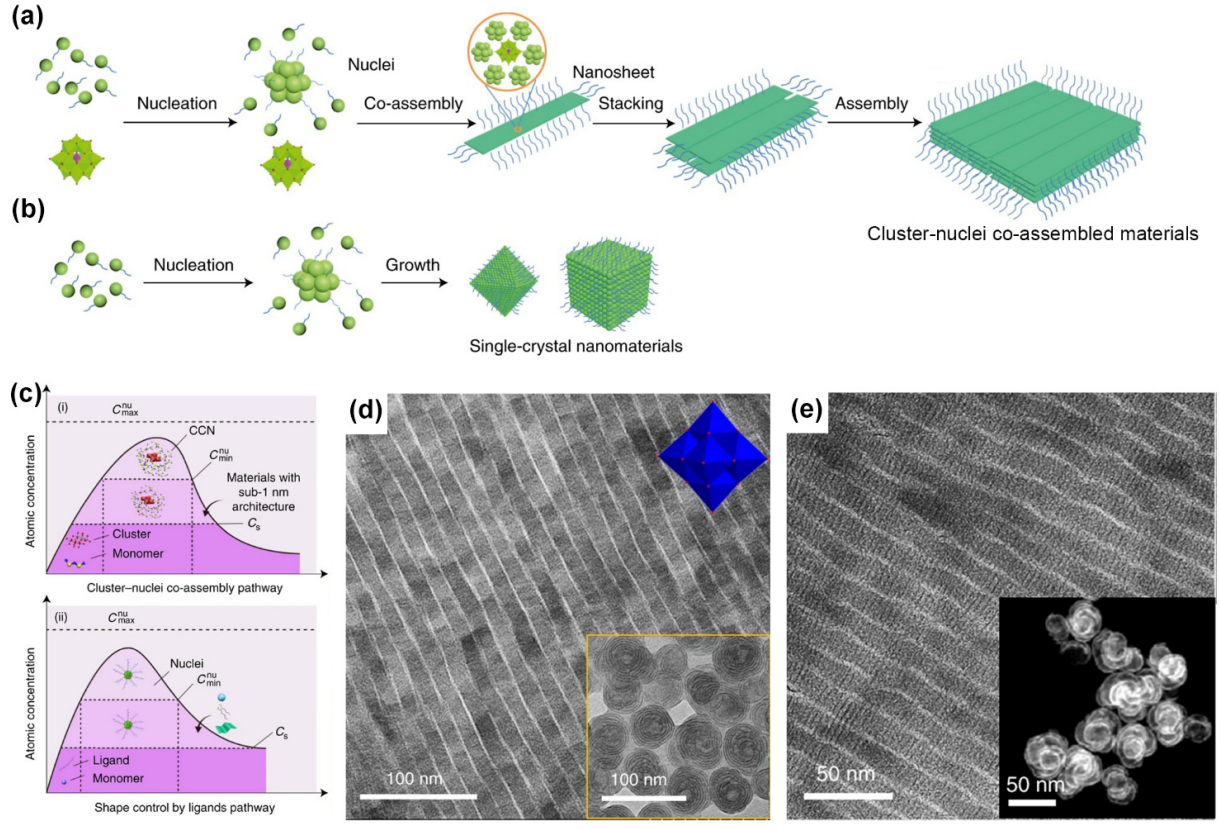

Figure 1 Scheme illustration of (a) cluster-nuclei co-assembly pathway and (b) the LaMer pathway (green sphere: monomers; green polyhedron: POM cluster; blue chains, ligands; green ribbon: sub-1 nm nanosheet). (c) Synthesis pathways for nanomaterials: (i) cluster-nuclei co-assembly (CCN: clusters and nucleus) and (ii) ligand-mediated shape control. (d) TEM image of NiS_x-NiO_x-POM (inset: TEM image of products when POMs are absent). (e) TEM image of NiCo-PMo_{12} (inset: high-angle annular dark-field scanning TEM (HAADF-STEM) image of products with the absence of POM). Reproduced with permission from Ref. [26], © Liu, J. L. et al., under exclusive licence to Springer Nature Limited 2019.

Akram et al. reported the single-step solvothermal syntheses of free-standing CoO-PMo_{12} ultrathin nanosheets (Fig. 2(a)) and single-walled nanotubes (Fig. 2(b)) [47]. Phosphomolybdic acid (PMo_{12}), oleylamine, ethanolamine, and Co acetate were used as precursors for the synthesis of CoO-PMo_{12} ultrathin (~ 2.0 nm thick) nanosheets, which were obtained after heating for 6 h at 180 °C and were well soluble in water and toluene because of their amphiphilicity. In a water–toluene mixture, these nanosheets self-assembled at the interface to afford two-dimensional (2D) Janus-like free-standing CoO-PMo_{12} ultrathin nanosheets. MD simulations revealed that the CoO nuclei assembled on top of the PMo_{12}–oleylamine layer (Fig. 2(c)), whereas inorganic nuclei surrounding PMo_{12} clusters were observed in other cases. Interestingly, CoO-PMo_{12} single-walled nanotubes were obtained in the absence of oleylamine (Fig. 2(b)). Unlike the corresponding nanosheets, these nanotubes were only sparingly soluble in ethanol. This approach was found to be rather versatile, i.e., Co ions could be replaced by Ni ions.

CoO-Mo_8 ultrathin nanowires were obtained when PMo_{12} was replaced by $[(^nC_4H_9)N]_4Mo_8O_{26}$ (Mo_8) in the CoO-POM system [48]. These results suggest that the morphology of MO_x-POM materials might be influenced by the composition or structure of POM clusters, highlighting the need to systematically study the coassembly of the same inorganic nucleus with various types of POMs. Liu et al. (2021) reported the coassembly of ZnO-$Zn(OH)_2$ with different POMs ($[(^nC_4H_9)N]_2Mo_6O_{19}$ (Mo_6), Mo_8, and PMo_{12}), which yielded three types of 2D ZnO-POM SNSs (ZnO-Mo_6, ZnO-Mo_8, and ZnO-PMo_{12}) [49]. TEM images (Figs. 2(d)–2(f)) indicated that these SNSs featured similar morphologies despite having notably different POM structures, in contrast to the CoO-POM system. The coassembly of MoO_3 or $Ni(OH)_2$ with various POMs is discussed in the following section.

Liu et al. used a one-pot solvothermal strategy to form 2D CuO PMo_{12} SNSs via the coassembly of CuO and PMo_{12} [50]. PMo_{12} and Cu nitrate were dissolved in ethanol, and the solution was supplemented with oleylamine and hexane, transferred into an autoclave, and heated at 140 °C for 4 h to obtain ~ 1 nm thick 2D CuO-PMo_{12} SNSs (Figs. 3(a)–3(c)). The distribution of inorganic nuclei and surface properties of these SNSs were different from those of CoO-PMo_{12} ultrathin nanosheets (which were constructed using one layer of CoO and one layer of PMo_{12}, as mentioned above). MD simulations revealed that in the 2D CuO-PMo_{12} SNSs, 12 CuO molecules stay in the vicinity of one PMo_{12} cluster. Unlike the amphiphilic CoO-PMo_{12} ultrathin nanosheets, the 2D CuO-PMo_{12} SNSs were hydrophobic and dispersible in cyclohexane. These differences in surface properties were ascribed to those in internal structures, which demonstrates that the internal structure of cluster-nuclei coassemblies directly governs their surface properties.

Beyond nanosheet structures, belt-like superstructures (ZrO_2-PMo_{12}, TiO_2-PMo_{12}, and MoO_3-POM) have been constructed utilizing ZrO_2, TiO_2, and MoO_3 as inorganic nuclei. Two kinds of ZrO_2-PMo_{12} nanobelts were reported. The first one was obtained without organic surfactants and featured PMo_{12} clusters attached to

Table 1 The reported cluster-nuclei assembled sub-1 nm materials

Entry	Assembly	Structure	Cluster	Nuclei
1	NiS_x-NiO_x-Mo_6 [26]	Nanosheet	$[(^nC_4H_9)N]_2Mo_6O_{19}$	NiS_x-NiO_x
2	NiS_x-NiO_x-Mo_6 [26]	Nanosheet	$[(^nC_4H_9)N]_4Mo_8O_{26}$	NiS_x-NiO_x
3	NiS_x-NiO_x-PMo_{12} [26]	Nanosheet	$H_3PMo_{12}O_{40}$	NiS_x-NiO_x
4	NiCo-Mo_8 [26]	Nanosheet	$[(^nC_4H_9)N]_4Mo_8O_{26}$	NiCo hydroxide
5	NiCo-PMo_{12} [26]	Nanosheet	$H_3PMo_{12}O_{40}$	NiCo hydroxide
7	CoO-PMo_{12} [47]	Nanosheet	$H_3PMo_{12}O_{40}$	CoO
8	CoO-PMo_{12} [47]	Nanotube	$H_3PMo_{12}O_{40}$	CoO
9	CoO-Mo_8 [48]	Nanowire	$[(^nC_4H_9)N]_4Mo_8O_{26}$	CoO
10	ZnO-Mo_6 [49]	Nanosheet	$[(^nC_4H_9)N]_2Mo_6O_{19}$	ZnO
11	ZnO-Mo_8 [49]	Nanosheet	$[(^nC_4H_9)N]_4Mo_8O_{26}$	ZnO
12	ZnO-PMo_{12} [49]	Nanosheet	$H_3PMo_{12}O_{40}$	ZnO
13	CuO-PMo_{12} [50]	nanosheet	$H_3PMo_{12}O_{40}$	CuO
14	ZrO_2-PMo_{12} [51]	Nanobelt	$H_3PMo_{12}O_{40}$	ZrO_2
15	TiO_2-PMo_{12} [51]	Nanobelt	$H_3PMo_{12}O_{40}$	TiO_2
16	MoO_3-W_6 [52]	Nanobelt	$[(^nC_4H_9)N]_2W_6O_{19}$	MoO_3
17	MoO_3-W_{10} [52]	Nanobelt	$[(^nC_4H_9)N]_4W_{10}O_{32}$	MoO_3
18	MoO_3-PW_{12} [52]	Nanobelt	$H_3PW_{12}O_{40}$	MoO_3
19	MnO-W_6 [53]	Nanobelt	$[(^nC_4H_9)N]_2W_6O_{19}$	MnO
20	MnO-W_{10} [53]	Nanobelt	$[(^nC_4H_9)N]_4W_{10}O_{32}$	MnO
21	MnO-PW_{12} [53]	Nanobelt	$H_3PW_{12}O_{40}$	MnO
22	Fe_2O_3-PMo_{12} [54]	Nanowire	$H_3PMo_{12}O_{40}$	Fe_2O_3
23	Y_2O_3-PMo_{12} [54]	Nanowire	$H_3PMo_{12}O_{40}$	Y_2O_3
24	Yb_2O_3-PMo_{12} [54]	Nanowire	$H_3PMo_{12}O_{40}$	Yb_2O_3
25	Bi_2O_3-PMo_{12} [54]	Nanowire	$H_3PMo_{12}O_{40}$	Bi_2O_3
26	CeO_2-PMo_{12} [54]	Nanowire	$H_3PMo_{12}O_{40}$	CeO_2
27	NiO-PMo_{12} [55]	Nanocoil	$H_3PMo_{12}O_{40}$	NiO
28	$MnZnCuO_x$-PMo_{12} [56]	Nanosheet	$H_3PMo_{12}O_{40}$	$MnZnCuO_x$
29	$CoZnCuNiFeZrCeO_x$-PMo_{12} [46]	Nanowire	$H_3PMo_{12}O_{40}$	$CoZnCuNiFeZrCeO_x$
30	$CoFeNiMnCuZnO_x$-PMo_{12} [57]	Nanobelt	$H_3PMo_{12}O_{40}$	$CoFeNiMnCuZnO_x$
31	$CoCrFeMnNiO_x$-PMo_{12} [58]	Nanobelt	$H_3PMo_{12}O_{40}$	$CoCrFeMnNiO_x$
32	$FeCoNiCrVO_x$-PMo_{12} [59]	Nanosheet	$H_3PMo_{12}O_{40}$	$FeCoNiCrVO_x$
33	$BiCuFeCeWPtO_x$-PMo_{12} [60]	Nanowire	$H_3PMo_{12}O_{40}$	$BiCuFeCeWPtO_x$
34	$Ni(OH)_2$-Mo_6 [61]	Nanowire	$[(^nC_4H_9)N]_2Mo_6O_{19}$	$Ni(OH)_2$
35	$Ni(OH)_2$-Mo_8 [61]	Nanowire	$[(^nC_4H_9)N]_4Mo_8O_{26}$	$Ni(OH)_2$
36	$Ni(OH)_2$-PMo_{12} [61]	Nanowire	$H_3PMo_{12}O_{40}$	$Ni(OH)_2$
37	$Ni(OH)_2$-$PMo_{11}Fe$ [62]	Nanowire	$H_6PMo_{11}FeO_{39}$	$Ni(OH)_2$
38	Cu_9S_5-PW_{12} [63]	Nanowire	$H_3PW_{12}O_{40}$	Cu_9S_5
39	Ni_3S_2-$FeMo_6$ [64]	Nanosheet	$(NH_4)_3[FeH_6Mo_6O_{24}]$	Ni_3S_2
40	Au-PW_{12} [44]	Nanowire	$H_3PW_{12}O_{40}$	Au
41	Ag-P_2W_{17} [65]	Nanowire	$K_{10}P_2W_{17}O_{62}$	Ag
42	Ag-P_2W_{15} [65]	Nanowire	$Na_{12}P_2W_{15}O_{56}$	Ag
43	Ag-EuW_{10} [65]	Nanowire	$Na_9EuW_{10}O_{36}$	Ag

the surface of ZrO_2-PMo_{12} nanobelts via van der Waals forces [66]. These ultrathin ZrO_2-PMo_{12} nanobelts (Fig. 3(d)) were flexible, probably because PMo_{12} acted as an inorganic surfactant within their structure, and exhibited a mesoporous structure with a large Brunauer–Emmett–Teller (BET) area of 222.88 $m^2 \cdot g^{-1}$, thus holding promise as catalysts for organic reactions. Sub-1 nm thick ZrO_2-PMo_{12} nanobelts of the second kind (Figs. 3(e)–3(g)) were synthesized using oleylamine as a surfactant and a good/poor solvent system (water/octadecene) [51]. Cryo-electron microscopy images showed that these nanobelts comprised ordered arrays of PMo_{12} clusters. MD simulations showed that the PMo_{12} clusters were assembled into arrays along the belts. Owing to their ultrathin structure, the ZrO_2-PMo_{12} nanobelts could confine octane and thus cause gel formation (inset of Fig. 3(e)). This synthetic system was

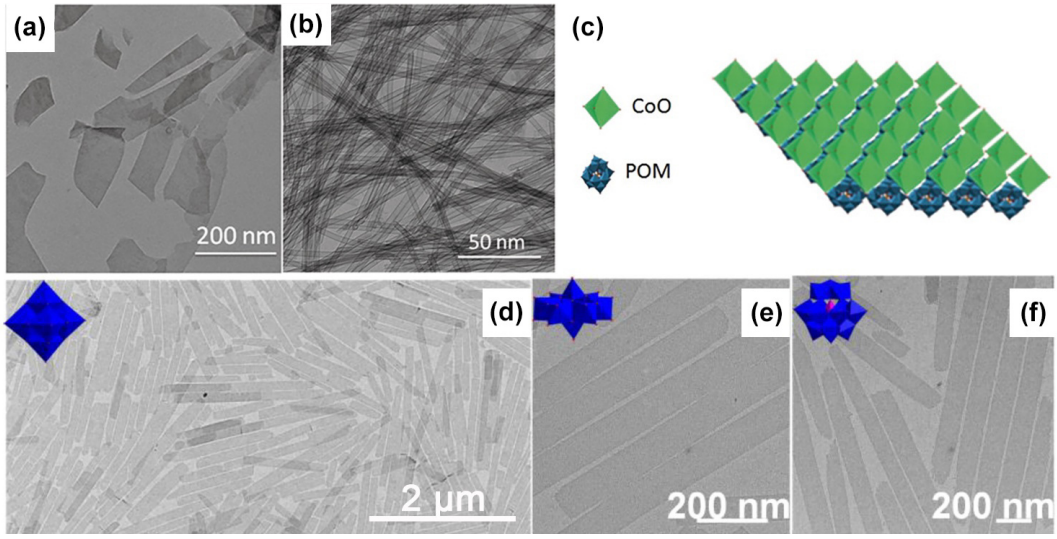

Figure 2 TEM images of the CoO-PMo_{12}: (a) nanosheets and (b) single-walled nanotubes. (c) Scheme of the CoO-PMo_{12} nanosheets. Reproduced with permission from Ref. [47], © Wiley-VCH Verlag GmbH & Co. KGaA, Weinheim 2019. TEM images of (d) ZnO-Mo_6, (e) ZnO-Mo_8, and (f) ZnO-PMo_{12} SNSs. Reproduced with permission from Ref. [49], © American Chemical Society 2021.

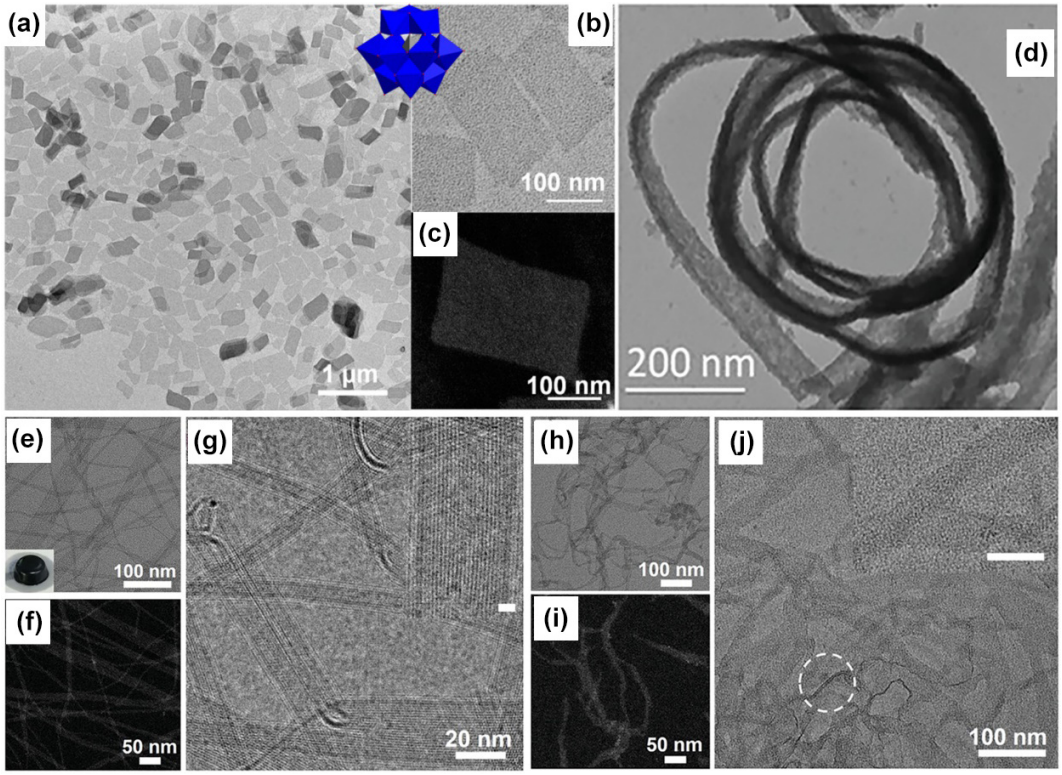

Figure 3 (a) and (b) TEM and (c) HAADF-STEM images of CuO-PMA SNSs. Reproduced with permission from Ref. [50], © American Chemical Society 2019. (d) TEM image of ZrO_2-PMo_{12} nanobelts. Reproduced with permission from Ref. [66], © WILEY-VCH Verlag GmbH & Co. KGaA, Weinheim 2019. (e) TEM, (f) HAADF-STEM, and (g) high-resolution TEM (HRTEM) images of ZrO_2-PMo_{12} sub-1 nm nanobelts (the inset in (e) shows a corresponding gel image). (h) TEM, (i) HAADF-STEM, and (j) HRTEM images of TiO_2-PMo_{12} sub-1 nm nanobelts. Reproduced with permission from Ref. [51], © Wiley-VCH GmbH 2021.

also applied to the synthesis of TiO_2-PMo_{12} sub-1 nm nanobelts (Figs. 3(h)–3(j)).

Liu et al. found that MoO_3 coassembled with different W-based POMs, namely $[(^nC_4H_9)N]_2W_6O_{19}$ (W_6), $[(^nC_4H_9)N]_4W_{10}O_{32}$ (W_{10}), phosphotungstic acid (PW_{12}), and silicotungstic acid, to form four types of MoO_3-POM sub-1 nm nanobelts [52]. TEM results of the sub-1 nm MoO_3-POM nanobelts showed that similarly to macromolecules, these nanobelts could bend, curl, and twist randomly. Cryo-electron microscopy images unveiled the nanobelts could coil and form spring-like structures. MD simulations revealed the interaction between POM clusters and MoO_3 in the nanobelts, with the introduction of POM clusters leading to bendability. Wang et al. (2022) prepared three types of MnO-POM nanobelts using W_6, W_{10}, and PW_{12} as POMs [53]. MnO nuclei coassembled with POM clusters into nanobelts under the synergistic effect of van der Waals and electrostatic interactions. Unlike the elongated and

flexible MoO_3-POM nanobelts, the MnO-POM nanobelts were much shorter, rigid, and unbendable.

Beyond nanosheets and nanobelts, MO_x-POM sub-1 nm nanowires were built through the coassembly of PMo_{12} clusters with Fe_3O_4, Y_2O_3, Yb_2O_3, Bi_2O_3, or CeO_2 as inorganic nuclei [54]. This strategy was found to be generally applicable to the synthesis of MO_x-POM nanowires. Moreover, these sub-1 nm nanowires exhibited polymer-like gelation behavior.

Fe_3O_4-POM and Bi_2O_3-POM sub-1 nm nanowires featured diameters and aspect ratios comparable with those of linear polymers and thus formed brown or blue gels when dispersed in cyclohexane. Owing to their polymer-analog properties, the Bi_2O_3-POM sub-1 nm nanowires could be processed into super-aligned films via wet spinning [67], which demonstrated that that cluster-nuclei coassembled materials can be processed similarly to polymers. The authors also tried to regulate the properties of Bi_2O_3-PMo_{12} nanowires via elemental (e.g., S and V) doping. NiO-PMo_{12} subnanocoils with a p-n-p-n-like configuration were also constructed [55].

3.2 HEO-POM

Although numerous metal oxides can coassemble with POM clusters to form ultrathin superstructures, it remains unclear whether different metal oxides can engage in coassembly with POM clusters in the same system. Multiple metal oxides (MnO, ZnO, and CuO) have been coassembled with PMo_{12} to afford $MnZnCuO_x$-PMo_{12} SNSs [56] with uniformly distributed Mn, Zn, and Cu (as evidenced by energy dispersive X-ray spectroscopy (EDS) mapping results). MD simulations indicated the stability of $MnZnCuO_x$-PMo_{12} SNSs, and each metal oxide had a relatively uniform distribution after simulation runs. Thus, this work reports novel sub-1-nm nanosheets with multiple components and an ideal method for expanding the scope of inorganic nuclei.

Building on the understanding of MO_x-POM systems, the cluster-nuclei coassembly mechanism could also be applied to HEO-POM systems. The introduction of compositional complexity in HEOs was pursued to modulate the electronic structure and enhance catalytic stability, addressing a key limitation of simple MO_x-POM systems. HEOs, which contain five or more metals, have attracted widespread attention [68, 69] because of their outstanding properties. The coassembly of HEOs and clusters presents three notable advantages: (i) Multiple metal cations enable the development of diverse HEO-POM materials with different properties [46]; (ii) the entropy effect can improve the stability of HEO-POM superstructures [62, 70]; and (iii) the synergistic effects between the components are responsible for emergent properties [60, 71].

As three kinds of metal oxides simultaneously coassemble with POM clusters, HEOs should also be utilized as inorganic nuclei to direct the coassembly of POM clusters into ordered superstructures. Dozens of HEO-POM superstructures have been reported and applied in catalysis, energy conversion, and energy storage. This section focuses on the compositions and structures of HEO-POM superstructures, with their applications discussed later.

The first HEO-POM (Figs. 4(a) and 4(b)) was developed by Wang et al. (2022) [46], who reported three kinds of HEO-PMo_{12} sub-1 nm nanowires (CuNiFeZrCeO_x-PMo_{12}, ZnCuNiFeZrCeO_x-PMo_{12}, and CoZnCuNiFeZrCeO_x-PMo_{12}) and constructed CeO_x-PMo_{12}, ZrCeO_x-PMo_{12}, FeZrCeO_x-PMo_{12}, and NiFeZrCeO_x-PMo_{12} sub-1 nm nanowires for comparison. The metal cations in HEOs were adjusted to obtain HEO-PMo_{12} sub-1 nm nanobelts, including FeNiMnCuZnO_x-PMo_{12} [57], CoFeNiMnCuZnO_x-PMo_{12} [57], CoCrFeMnNiO_x-PMo_{12} [58], and FeCoNiCrVO_x-PMo_{12} ones (Figs. 4(c) and 4(d)) [59]. Nie et al. prepared high-entropy $LaMnO_3$-type perovskite (HELMO)-POM subnanowires via cluster-nuclei coassembly. The HELMO contained six metal ions (La^{3+}, Cr^{3+}, Mn^{3+}, Fe^{3+}, Co^{2+}, and Ni^{2+}) [72]. Once HELMO nuclei formed in the solvothermal reaction, they coassembled with POM (PW_{12}) clusters to form the heterounits shown in Fig. 4(e). The uniform diameter (1.8 nm) of the HELMO-POM subnanowires was attributed to the presence of POM clusters (Fig. 4(f)). HELMO nanowires synthesized without POM clusters lacked this size constraint and therefore featured an uneven diameter distribution. Notably, the HELMO-POM subnanowires were prepared at a temperature (100 °C) substantially lower than those typically required for synthesizing HEOs. Pt cations were introduced into HEO-POM sub-1 nm nanowires to afford a composition of BiCuFeCeWPtO_x-PMo_{12} (Figs. 4(g) and 4(h)) [60]. Owing to the diversity of HEOs, a notable increase in the number of reported HEO-PMo_{12} systems is expected in the near future.

3.3 MOH_x-POM

Metal hydroxides represent a compelling class of inorganic nuclei. According to the cluster-nuclei coassembly mechanism, many kinds of metal hydroxide nuclei can coassemble with POM clusters. However, only $Ni(OH)_2$ has been adopted to coassemble with POMs to date. Liu et al. synthesized $Ni(OH)_2$-PMo_{12} sub-1 nm nanowires using $NiCl_2$ and PMo_{12} as precursors (Fig. 5(a)) [61]. With decreasing addition of $NiCl_2$, $Ni(OH)_2$-PMo_{12} sub-1 nm nanobelts were obtained (Fig. 5(b)). Mo_6 and Mo_8 were also coassembled with $Ni(OH)_2$ nuclei to form $Ni(OH)_2$-Mo_6 and $Ni(OH)_2$-Mo_8 sub-1 nm nanowire assemblies (Figs. 5(c) and 5(d)). MD simulations were performed to explore assembly mechanisms. The $Ni(OH)_2$-PMo_{12} sub-1 nm nanobelts had a simple square structure, whereas $Ni(OH)_2$-Mo_6 and $Ni(OH)_2$-Mo_8 sub-1 nm nanowire assemblies had a body-centered cubic structure. The MD simulation and experimental results indicated that all $Ni(OH)_2$-POM sub-1 nm superstructures were stable.

Metal-substituted POMs [73, 74] were synthesized by reacting metal (e.g., Ru, Pd, Ir, and Co) cations with lacunary POMs [29, 75–77]. According to the structural similarity of metal-substituted and nonsubstituted POMs, the former should act as clusters during cluster-nuclei coassembly. Recently, a metal-substituted POM ($H_6PMo_{11}FeO_{39}$, denoted as $PMo_{11}Fe$) has been used for the first time to coassemble with $Ni(OH)_2$ (Figs. 5(e) and 5(f)) [62], which expands the scope of POM clusters. The synthesis of $Ni(OH)_2$-$PMo_{11}Fe$ sub-1 nm nanowires was similar to that of $Ni(OH)_2$-PMo_{12} ones except for the use of $PMo_{11}Fe$ instead of PMo_{12}. High-resolution TEM (HRTEM) and atomic force microscopy analyses indicated that the $Ni(OH)_2$-$PMo_{11}Fe$ nanowires had sub-1 nm characteristics. The formation process of these nanowires was revealed by MD simulations and found to be driven by electrostatic interactions. More importantly, Fe atoms were found to be spatially integrated into the nanowire structure, which could be viewed as an atomically dispersed catalyst. Therefore, the introduction of metal-substituted POMs into cluster-nuclei assembly will broaden the scope of sub-1 nm superstructures and their applications.

3.4 MS_x-POM

Metal sulfides share certain properties with metal oxides, adopting identical or closely related crystal structures, and should therefore

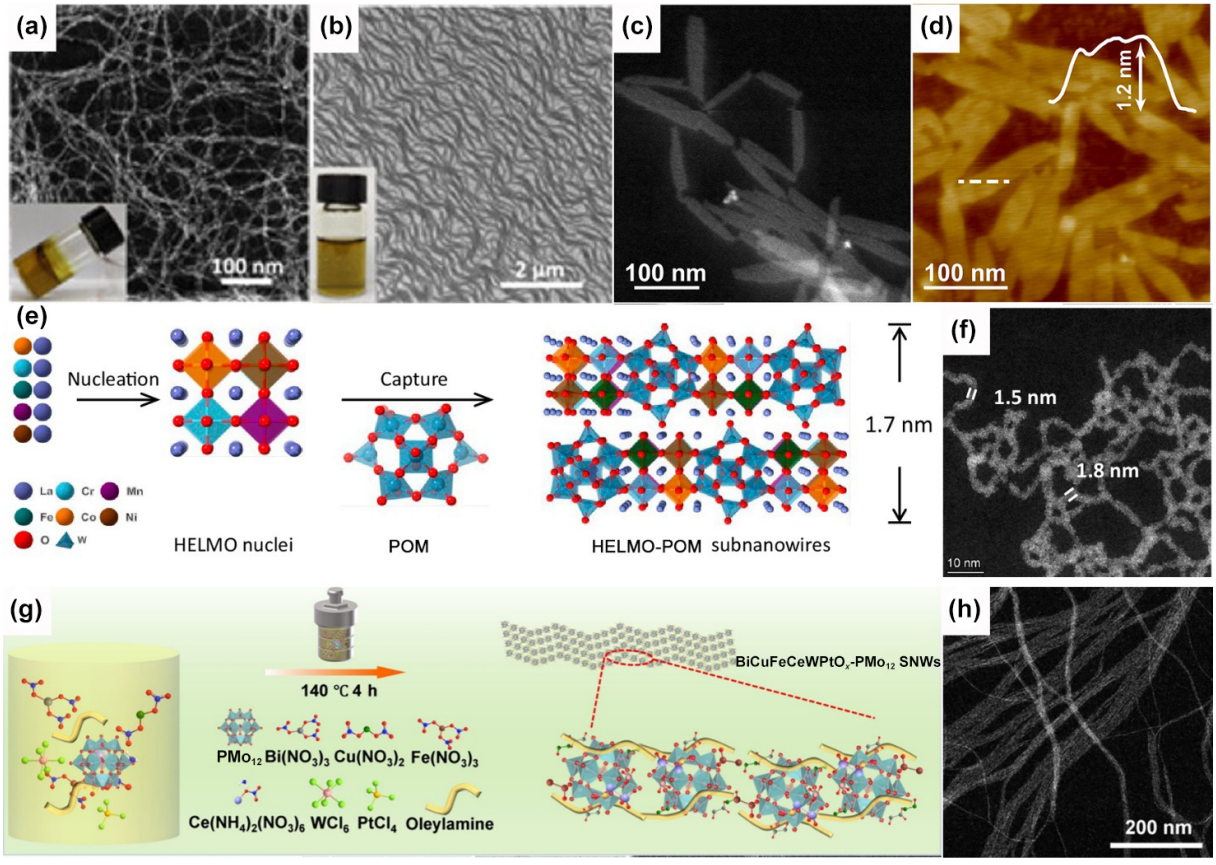

Figure 4 HEO-POM co-assemblies. (a) HAADF-STEM and (b) TEM images of $CuNiFeZrCeO_x$-PMo_{18} sub-1 nm nanowires. The insets in (a) and (b) show the corresponding gel images. Reproduced with permission from Ref. [46], © American Chemical Society 2022. (c) HAADF-STEM and (d) AFM images of $FeCoNiCrVO_x$-PMo_{12} SNSs. Reproduced with permission from Ref. [59], © Science China Press 2025. (e) Scheme illustration of the formation and (f) HAADF-STEM image of HELMO-POM subnanowires. Reproduced with permission from Ref. [72], © Nie, S. Y. et al. 2024. (g) Scheme illustration of the formation and (h) HAADF-STEM image of $BiCuFeCeWPtO_x$-PMo_{12}. Reproduced with permission from Ref. [60], © American Chemical Society 2025.

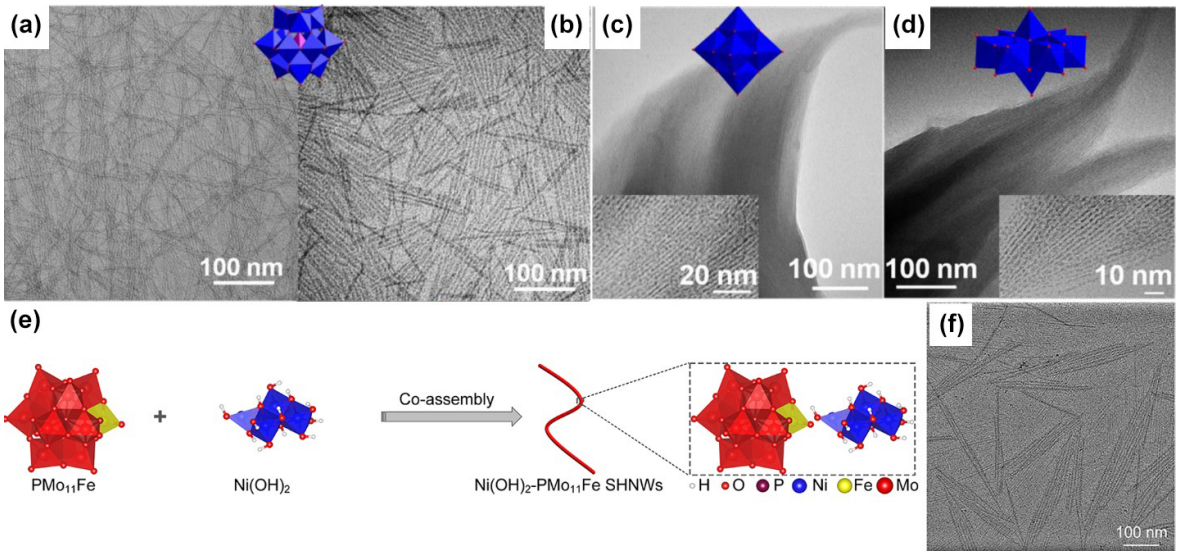

Figure 5 TEM images of (a) $Ni(OH)_2$-PMo_{12} sub-1 nm nanowires, (b) $Ni(OH)_2$-PMo_{12} sub-1 nm nanobelts, and (c) $Ni(OH)_2$-Mo_6 and (d) $Ni(OH)_2$-Mo_8 sub-1 nm nanowires (insets: HRTEM images). Reproduced with permission from Ref. [61], © American Chemical Society 2021. (e) Scheme of the synthesis process and (f) TEM image of $Ni(OH)_2$-$PMo_{11}Fe$ sub-1 nm nanowires. Reproduced with permission from Ref. [62], © Wiley-VCH GmbH 2025.

be excellent inorganic nuclei for cluster-based assembly. However, only several types of metal sulfides have been successfully coassembled with POM clusters thus far.

One example is the coassembly of Cu_9S_5 with PW_{12} affording Cu_9S_5-PW_{12} sub-1 nm nanowires (Figs. 6(a) and 6(c)) [63]. Without the addition of PW_{12} clusters, Cu_9S_5 nanowires with a diameter of 24 nm were obtained (Figs. 6(b) and 6(d)). Therefore, the introduction of PW_{12} clusters was essential for confining nanowire

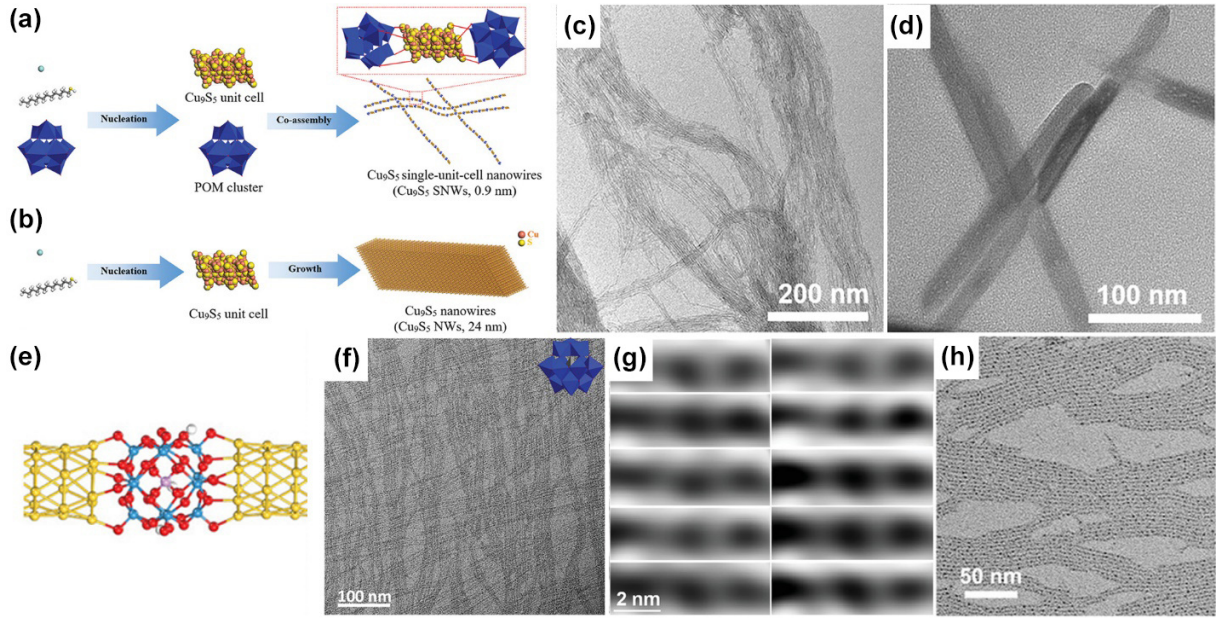

Figure 6 Scheme of synthesis process of (a) Cu_9S_5-PW_{12} sub-1 nm nanowire and (b) Cu_9S_5 nanowire. TEM images of (c) Cu_9S_5-PW_{12} sub-1 nm nanowire and (d) Cu_9S_5 nanowire. Reproduced with permission from Ref. [63], © Wiley-VCH GmbH 2021. (e) Model of Au-PW_{12} building block. (f) TEM and (g) Cryo-TEM images of Au-PW_{12} sub-1 nm nanowires. Reproduced with permission from Ref. [44], © Wiley-VCH GmbH 2020. (h) TEM image of Ag-P_2W_{17} nanowires. Reproduced with permission from Ref. [65], © Wiley-VCH GmbH 2022.

growth to the sub-1 nm level. The diameter of the sub-1 nm nanowires (~ 0.9 nm) closely matched the unit cell size of Cu_9S_5 (~ 0.893 nm), which suggested that the single-unit cell of Cu_9S_5 connected with a PW_{12} cluster via Cu–O bonding to form an A-B (Cu_9S_5-PW_{12}) building block. Subsequently, these blocks assembled in one dimension to generate a continuous A-B-A-B chain-like structure. This assembly mirrored a polymerization process, with PW_{12} clusters and Cu_9S_5 single-unit cells acting as monomers, and afforded Cu_9S_5-PW_{12} sub-1 nm nanowires. Therefore, these nanowires can be viewed as a single-unit-cell structure, which has demonstrated outstanding catalytic performance.

Ni_3S_2-$FeMo_6$ SNSs were reported [64]. $(NH_4)_3[FeH_6Mo_6O_{24}]\cdot 7H_2O$ ($FeMo_6$) clusters, another kind of Fe-substituted Ander-type POMs, were introduced into the nucleation process of Ni_2S_3 to generate the superlattice structure of Ni_3S_2-$FeMo_6$ SNSs. In this work, Ni_3S_2-$(NH_4)_6[Mo_7O_{24}]$ (Ni_3S_2-Mo_7) nanosheets were synthesized as a control sample using $(NH_4)_6[Mo_7O_{24}]$ as POM clusters. Compared with the superlattice structure of Ni_3S_2-$FeMo_6$, the Ni_3S_2-Mo_7 SNSs exhibited a lower degree of structural ordering, which indicates that even a slight variation in the POM clusters can markedly alter the morphology of the final product.

3.5 NM-POM

NM (Au, Pt, Pd, Ru, and Ag) nanoparticles and clusters are the most studied inorganic nanomaterials because (i) their electronic structures result in high catalytic activity in a wide variety of reactions [78], including electrocatalytic and organic ones, and (ii) their size and shape can be easily controlled [79].

Moreover, these nanoparticles/clusters have long-term stability in many catalytic processes because of their resistance to oxidation and corrosion. Numerous NM particles/clusters have been reported, e.g., Au nanorods [80], Au clusters [81], Au-Ag nanoboxes [82], and Pd nanocubes [83]. In 2009, Au nanocrystals were coassembled with POMs under the action of electrostatic interactions [35]. Unlike cluster-nuclei coassembly, this process proceeded without any interaction between Au nanocrystals and POMs.

Liu et al. (2021) constructed A-B-A-B-type Au-PW_{12} sub-1 nm nanowires (Figs. 6(e) and 6(f)) [44], where A stands for Au cluster and B stands for PW_{12}, as in the abovementioned case of Cu_9S_5-PW_{12}. Figure 6(g) shows a cryo-electron microscopy image confirming this A-B-A-B structure. Electron transfer between PW_{12} and the Au cluster was demonstrated, with the former and latter functioning as an electron donor and acceptor, respectively. This electron transfer reinforced the interaction between PW_{12} and the Au cluster, contributing to the superior stability of the Au-PW_{12} sub-1 nm nanowires. Three kinds of Ag-POM sub-1 nm nanowires (Ag-P_2W_{17}, Ag-P_2W_{15}, and Ag-EuW_{10}) were synthesized via an atypical cluster-nucleation coassembly of Ag species and POMs facilitated by light under nonsolvothermal conditions [65]. POMs and $AgNO_3$ were dissolved in deionized water, and the solution was dropwise supplemented with that of cetrimonium bromide in chloroform. Finally, the mixture was subjected to 12 h of stirring under visible-light irradiation. During irradiation, Ag^+ was *in situ* reduced to Ag clusters on the POM cluster surface. The Ag clusters acted as linkers between POM clusters, enabling the construction of an A-B-A-B (A: Ag, B: POM) structure, as revealed by low-magnification TEM image (Fig. 6(h)). This straightforward and energy-efficient synthetic method might provide a general route to new functional materials.

3.6 Other coassemblies

All abovementioned materials, including MO_x-POM, HEO-POM, MOH-POM, MS_x-POM, and NM-POM, are binary coassemblies. Ternary metal oxysulfide-POM-metal cluster coassemblies were constructed in the early stages of discovering coassembled materials. Wang et al. (2019) first reported the cluster-nuclei coassembly strategy [26], coassembling POMs (Mo_6, Mo_8, and PMo_{12}) with Ni oxysulfide (NiS_x-NiO_x) or NiCo hydroxide nuclei to afford binary coassemblies, namely NiS_x-NiO_x-Mo_6, NiS_x-NiO_x-

Mo_8, NiS_x-NiO_x-PMo_{12}, NiCo-Mo_8, and NiCo-PMo_{12}. The TEM results of NiS_x-NiO_x-Mo_6, NiS_x-NiO_x-Mo_8, and NiS_x-NiO_x-PMo_{12} showed that these binary coassemblies were uniform in size and shape. Hollow NiS_x-NiO_x spheres were obtained without POMs. NiS_x-NiO_x-Mo_8-PtP, NiS_x-NiO_x-PMo_{12}-PtP, NiS_x-NiO_x-Mo_6-Au-Ag, NiS_x-NiO_x-Mo_6-Au-Ag, NiS_x-NiO_x-PMo_{12}-Pd, and NiS_x-NiO_x-PMo_{12}-Ag ternary coassemblies were synthesized by adding NM nanoclusters (PtP, Pd, Au, and Ag clusters) to ethanolic solutions of binary assemblies. Numerous uniform lattices never found on binary coassemblies were observed on each strip of ternary coassemblies. To reveal the formation mechanism of these ternary coassemblies, the authors analyzed changes in nanoclusters during the reaction using MALDI-TOF-MS and time-dependent ultraviolet absorption spectroscopy. The synthesized nanoclusters were found to contain much smaller clusters capable of entering the structure of binary coassemblies. As the reaction progressed and the consumption of the smaller clusters increased, the larger clusters began to dissolve into smaller clusters and inserted into binary coassemblies to continually form ternary coassemblies. Therefore, the formation of ternary coassemblies was concluded to involve a precipitation–dissolution process. MD simulations confirmed this conclusion and revealed that this process was driven by van der Waals interactions.

Wang et al. introduced Au nanoparticles into the coassembly of a CoNi layered double hydroxide (LDH) and PMo_{12} to synthesize CoNi LDH-PMo_{12}-Au SNSs via the precipitation–dissolution mechanism [84]. MD simulations revealed that charge transfer between Au and the nanosheets accelerated the dissolution of Au nanoparticles into smaller Au clusters, and the interaction between Au and PMo_{12} was found to be stronger than that between Au and the CoNi LDH. Therefore, CoNi LDH-PMo_{12}-Au SNSs showed enhanced stability. The same method was used to synthesize CoNi LDH-PMo_{12}-Ag and CoNi LDH-PMo_{12}-Pd SNSs.

However, not all ternary coassemblies formed via precipitation–dissolution mechanism, Liu et al. (2021) prepared CuO-PMo_{12}-Ag sub-1 nm nanosheet heterostructures by introducing Ag nanoparticles into a cyclohexane solution of CuO-PMo_{12} nanosheets [85]. However, the Ag nanoparticles could only be observed at the nanosheet edges. The interaction between the CuO-PMo_{12} nanosheets and Ag nanoparticles was studied by MD simulations, which showed that after undergoing random motion, the Ag nanoparticles primarily attached to nanosheet edges to afford energetically favorable heterostructures and hence, stable CuO-PMo_{12}-Ag SNSs.

4 Applications of cluster-nuclei assemblies

Cluster-nuclei assemblies find numerous applications, including photo/electro-catalytic reactions, catalytic organic reactions, energy storage, solar steam generation, seawater desalination, and tumor treatment. Ultrathin materials with sub-1 nm sizes exhibit unique properties, such as high surface-to-volume ratios, maximized atomic exposure, and electronic delocalization, thus showing high catalytic activity and superior charge transport or storage capacity in battery applications.

4.1 Catalysis of organic reactions

POMs have been used to catalyze several organic reactions, including thioether oxidation, alkene epoxidation, and alcohol oxidation. Therefore, nuclei-POM coassemblies could also serve as catalysts for these reactions. Furthermore, owing to the synergistic effect between the inorganic nuclei and POMs, these coassemblies exhibit catalytic activities exceeding those of POMs.

4.1.1 *Oxidation of thioethers*

Thioether oxidation, also referred to as oxidative desulfurization (ODS), is used to remove sulfur from gasoline. Owing to the oxidative capability of POMs, nuclei-POM coassemblies serve as active ODS catalysts (Fig. 7) enhancing the selectivity for sulfones and increasing conversion. NiCo-PMo_{12} and NiCo-Mo_8 nanosheets achieved 100% conversion and 100% selectivity in the oxidation of dibenzothiophene to the corresponding sulfone at room temperature within 20 min [26]. Further studies demonstrated that most MO_x-POM coassemblies, including ZrO_2-PMo_{12} nanobelts [66], MoO_3-PMo_{12} sub-1 nm nanobelts [52], ZrO_2/TiO_2-PMo_{12} sub-1 nm nanobelts [51], ZnO-Mo_6/Mo_8/PMo_{12} SNSs [49], and Ag-P_2W_{17} nanowires [65], efficiently catalyze ODS under mild conditions.

4.1.2 *Alkene epoxidation*

Given the ability of POMs to catalyze alkene epoxidation, MO_x-POM coassemblies were employed as catalysts for styrene and cyclohexene epoxidation. For styrene epoxidation [47], the reaction system included CoO-PMo_{12} ultrathin nanosheets (25 mg), styrene (2.5 mmol), acetonitrile (solvent; 5 mL), and *tert*-butyl hydroperoxide (oxidant; 7.5 mmol), with the reaction carried out at 75 °C. After 15 h, the conversion and selectivity reached 94% and 96%, respectively, notably exceeding those achieved for pure PMo_{12} or CoO. Liu et al. found that the ternary coassembly of CuO-PMo_{12}-Ag catalyzed the epoxidation of alkenes, e.g., cyclohexene, 1-octane, and *cis*-stilbene [85]. Chloroform and iodosobenzene were used as the solvent and oxidant, respectively, and complete conversion (> 99%) and perfect selectivity (100%) were achieved for all three alkenes at 50 °C.

4.1.3 *Oxidation of alcohols to aldehydes*

In addition to promoting the oxidation of thioethers and alkenes, MO_x-POM also catalyze that of alcohols. MnO-POM nanosheets with different POM clusters (W_6, W_{10}, and PW_{12}) were found to catalyze the oxidation of benzyl alcohols to benzaldehydes [53], achieving higher conversions and selectivities at lower temperatures compared with many reported catalysts. When *p*-nitrobenzyl alcohol was used as the substrate, the conversion reached 100%, and the reaction time sharply decreased. Density functional theory (DFT) calculations shed light on the reactivity of MnO-POM catalysts. Bader charge analysis indicated that the Mn atoms in MnO-W_6 were slightly oxidized compared with those of pure MnO, contributing to the higher activity of MnO-POM. The energy barrier of the rate-determining step (RDS) for MnO-W_6 was

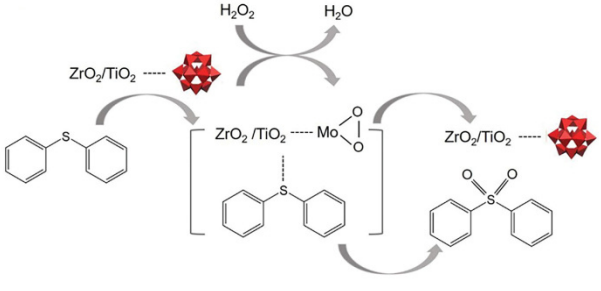

Figure 7 Mechanism for the oxidation of thioethers catalyzed by the ZrO_2/TiO_2-PMo_{12}. Reproduced with permission from Ref. [51], © Wiley-VCH GmbH 2021.

lower than that for pure MnO, resulting in enhanced catalytic activity.

4.2 Photo/electro-catalysis

4.2.1 CO_2 reduction

Photo/electro-catalytic CO_2 reduction has been thoroughly studied and affords CO as the most favorable product. CoO-Mo_8 nanowires were found to catalyze the photoreduction of CO_2 and H_2O to syngas (CO and H_2), delivering a CO/H_2 evolution rate of 4165/11,555 mmol·g^{-1}·h^{-1} [48]. For pure CoO nanowires, the CO/H_2 evolution rate under light irradiation was 3112/12,855 mmol·g^{-1}·h^{-1}. The presence of Mo_8 in CoO-Mo_8 nanowires enhanced the productivity of CO and thus benefited syngas utilization. Cluster-nuclei assemblies can also drive electrocatalytic CO_2 reduction. For example, when Cu_9S_5-PW_{12} sub-1 nanowires were used as an electrocatalyst for CO_2 reduction, the main product ($HCOO^-$) was obtained with a maximum Faradaic efficiency (FE) of 82.0% at −0.8 V [63]. When Cu_9S_5 nanowires with a diameter of 24 nm were used, the main product (ethanol) was produced with a maximum FE of 21.5% at −0.9 V. These results indicate that POM clusters can regulate the catalytic performance of coassemblies. Liu et al. reported that Au-PW_{12} sub-1 nm assemblies accelerated electrocatalytic CO_2 reduction to CO [44]. This reduction was further enhanced by light irradiation, with the FE of CO formation reaching 99% at −0.7 to −0.9 V.

4.2.2 Oxygen evolution reaction (OER)

Nuclei–cluster coassemblies such as HEO-POM can also serve as highly efficient electrocatalysts for the OER [59]. FeCoNiCrVO_x-PMo_{12} SNSs required an overpotential of only 229 mV to reach a current density of 10 mA·cm^{-2} and exhibited exceptional operational stability, sustaining their electrocatalytic activity for > 1000 h at a high current density of 250 mA·cm^{-2}. DFT calculations revealed that composition engineering could accelerate the OER, with Co identified as the active site and Ni, V, and Fe coordination lowering reaction barriers. Therefore, the FeCoNiCrVO_x-PMO_{12} SNSs exhibited the lowest energy barrier among all control samples. Moreover, the sub-1 nm structural design improved the long-term stability for the OER.

He et al. found that the electrocatalytic activity of nuclei-cluster coassemblies can be regulated by adjusting cluster composition [62]. Ni$(OH)_2$-PMo_{11}Fe sub-1 nm nanowires were constructed by substituting PMo_{12} with PMo_{11}Fe in the Ni$(OH)_2$-PMo_{12} system and required an overpotential of only 290 mV to deliver a current density of 50 mA·cm^{-2}, which was much lower than that required by Ni$(OH)_2$-PMo_{12} nanowires (424 mV). More importantly, DFT calculation results indicated that the rate-determining step for the OER was different when catalyzed by Ni$(OH)_2$-PMo_{11}Fe vs. Ni$(OH)_2$-PMo_{12}. And the energy barrier for the RDS of Ni$(OH)_2$-PMo_{11}Fe was lower than that of Ni$(OH)_2$-PMo_{12}. Differential charge density analysis and Bader charge calculations demonstrated that the incorporation of Fe decreased electron density around Ni. These results explain the higher electrocatalytic activity of Ni$(OH)_2$-PMo_{11}Fe for the OER. Ni_3S_2-$FeMo_6$ nanosheets were synthesized and compared with Ni_3S_2-$(NH_4)_6Mo_7O_{24}$ (Ni_3S_2-Mo_7) [64]. The former nanosheets required a much lower overpotential of 342 mV to deliver a current density of 100 mA·cm^{-2} and could be stably operated for > 100 h. For Ni_3S_2-Mo_7, the overpotential required to reach 100 mA·cm^{-2} (> 500 mV) notably exceeded that observed for Ni_3S_2-$FeMo_6$, which underscores the critical role of Fe incorporation in the POM for enhancing the OER activity.

The outstanding OER performance of Ni$(OH)_2$-PMo_{11}Fe and Ni_3S_2-$FeMo_6$ indicated that the composition regulation of POM clusters in nuclei-cluster coassemblies enables property and performance adjustment.

The CoFeNiMnCuZnO$_x$-PMo_{12} nanosheets exhibited good electrocatalytic performance for the OER (Figs. 8(a) and 8(b)) [57]. Upon illumination, this catalyst delivered an overpotential of 165 mV at a current density 10 mA·cm^{-2}, which was lower than that measured without light and those of many reported electrocatalysts. Therefore, CoFeNiMnCuZnO$_x$-PMo_{12} SNSs acted as a photoelectrocatalyst for the OER, which could further enhance catalytic activity.

4.2.3 Oxygen reduction reaction (ORR)

The CoFeNiMnCuZnO$_x$-PMo_{12} SNSs could also serve as a photoelectrocatalyst for the ORR (Figs. 8(c) and 8(d)) [57]. The half-wave potential of these nanosheets under light (0.802 V) exceeded those of control samples, and the corresponding Tafel slope (67.8 mV·dec^{-1}) was lower than those of NiMnCuZnO$_x$-PMo_{12} and FeNiMnCuZnO$_x$-PMo_{12} nanosheets. The ORR performance of CoFeNiMnCuZnO$_x$-PMo_{12} was superior to those of pure PMo_{12}, CoFeNiMnCuZnO$_x$, and commercial RuO_2, which was attributed to its larger electrochemical surface area.

4.2.4 Urea oxidation

HEO-POM coassemblies are efficient electrocatalysts for the OER and ORR. Based on mechanistic similarity considerations, their application can be extended to electrocatalytic urea oxidation, which is a promising alternative to the OER for reducing the energy cost of hydrogen production. Cheng et al. found that CoCrFeMnNiO$_x$-PMo_{12} nanobelts are an excellent electrocatalyst for urea oxidation [58]. When applied to the OER, the nanobelts required a potential of 1.55 V to deliver a current density of 10-mA·cm^{-2} in 1.0 M KOH. For urea oxidation, when 0.33 M urea was introduced, the nanobelts exhibited a potential of 1.34 V at 10 mA·cm^{-2} and could stably operate for 24 h. DFT calculations, including charge difference analysis, projected density of states analysis, adsorption energies, and Gibbs free energy diagrams, revealed the origin of this outstanding catalytic performance, ascribing it to electron delocalization.

4.2.5 Photoelectrocatalytic methane oxidation

The oxidative activation of methane remains challenging. Sub-1-nm materials with ultrahigh surface areas have the potential to be good catalysts for methane oxidation. Nie et al. found that NiO-PMo_{12} subnanocoils exhibited outstanding performance in the photoelectrocatalytic oxidative coupling of CH_4 to oxalate at room temperature and atmospheric pressure, delivering an oxalate productivity of 4.48 mmol·g_{cat}^{-1}·h^{-1} and a selectivity of > 99% (Fig. 9) [55]. The mechanism of this oxidative coupling was revealed by *in situ* Fourier transform infrared spectroscopy (FTIR), *in situ* electron paramagnetic resonance spectroscopy, and DFT calculations. Electron state delocalization was suggested to stabilize the adsorbate and reduce the energy barrier of the reaction.

4.3 Batteries

Nuclei-cluster assemblies are widely used in batteries, including Li-ion, Na-ion, Li-S, Li-O_2, and Zn-air batteries, and can function as anode materials, cathode catalysts, and separators.

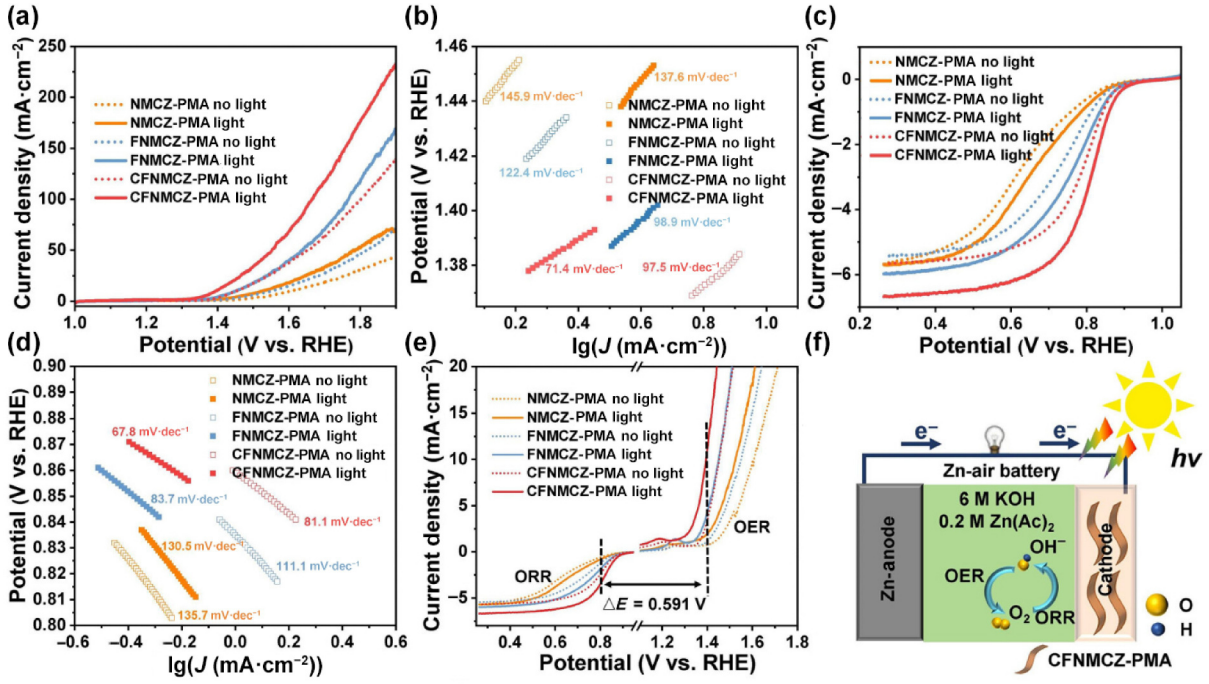

Figure 8 Polarization curves for (a) OER (1 M KOH) and (c) ORR (0.1 M KOH) at 1600 rpm. Corresponding Tafel slopes for (b) OER and (d) ORR. (e) Combined OER/ORR polarization profile representing overall oxygen electrocatalytic activity. (f) Scheme illustration of Zn-air battery based on CoFeNiMnCuZnO$_x$-PMo$_{12}$. (NMCZ-PMA, NiMnCuZnO$_x$-PMo$_{12}$; FNMCZ-PMA, FeNiMnCuZnO$_x$-PMo$_{12}$; CFNMCZ-PMA, CoFeNiMnCuZnO$_x$-PMo$_{12}$). Reproduced with permission from Ref. [57], © American Chemical Society 2024.

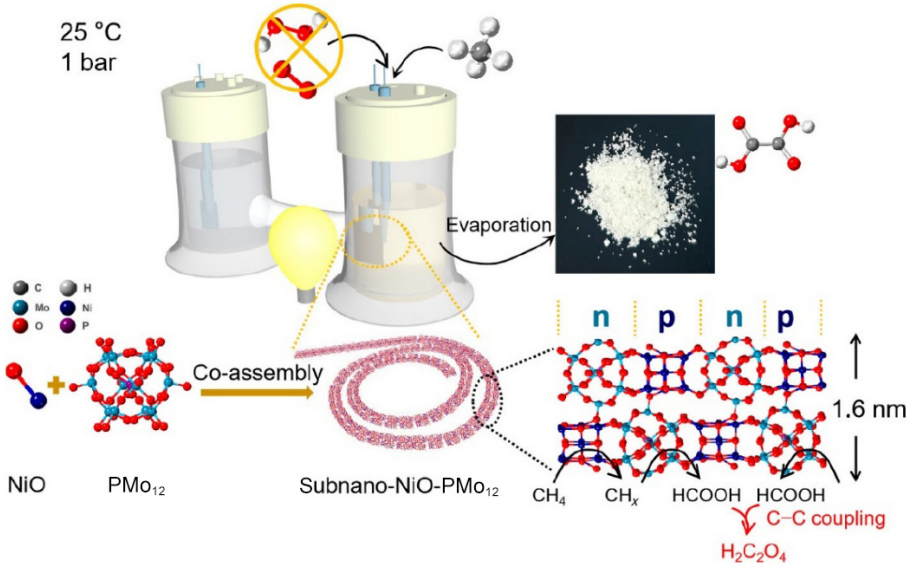

Figure 9 Scheme of the direct photoelectrocatalytic coupling of CH_4 to oxalate. The process, facilitated by NiO-PMo$_{12}$ subnanocoils, proceeds under ambient conditions without added oxidants. Reproduced with permission from Ref. [55], © American Chemical Society 2023.

4.3.1 Li-ion batteries

Yuan et al. prepared MnZnCuO$_x$-PMo$_{12}$ SNSs using varying amounts of PMo$_{12}$ (0.018, 0.036, 0.054, and 0.072 g), denoting the products as MnZnCuO$_x$-PMo$_{12}$-0.018, MnZnCuO$_x$-PMo$_{12}$-0.036, MnZnCuO$_x$-PMo$_{12}$-0.054, and MnZnCuO$_x$-PMo$_{12}$-0.072 nanosheets, respectively [56]. These nanosheets were evaluated as Li-ion battery anode materials (Fig. 10). Compared with pure MnZnCuO$_x$ and PMo$_{12}$, the MnZnCuO$_x$-PMo$_{12}$ nanosheets exhibited a higher initial discharge/charge capacity, which indicated the existence of a synergistic effect between MnZnCuO$_x$ and PMo$_{12}$.

MnZnCuO$_x$-PMo$_{12}$-0.036 showed the highest initial discharge and charge capacities of 2177 and 945 mAh·g^{-1}, respectively (Fig. 10(a)). Furthermore, the MnZnCuO$_x$-PMo$_{12}$-0.036 nanosheets exhibited an excellent rate performance, maintaining a high capacity even at high current densities (Fig. 10(c)). The long-term cycling stability of the MnZnCuO$_x$-PMo$_{12}$-0.036 nanosheets notably exceeded that of the other samples (Figs. 10(d) and 10(e)). Moreover, the structure and morphology of the MnZnCuO$_x$-PMo$_{12}$-0.036 nanosheets were maintained after cycling. Therefore, these SNSs might be promising anode materials for Li-ion batteries.

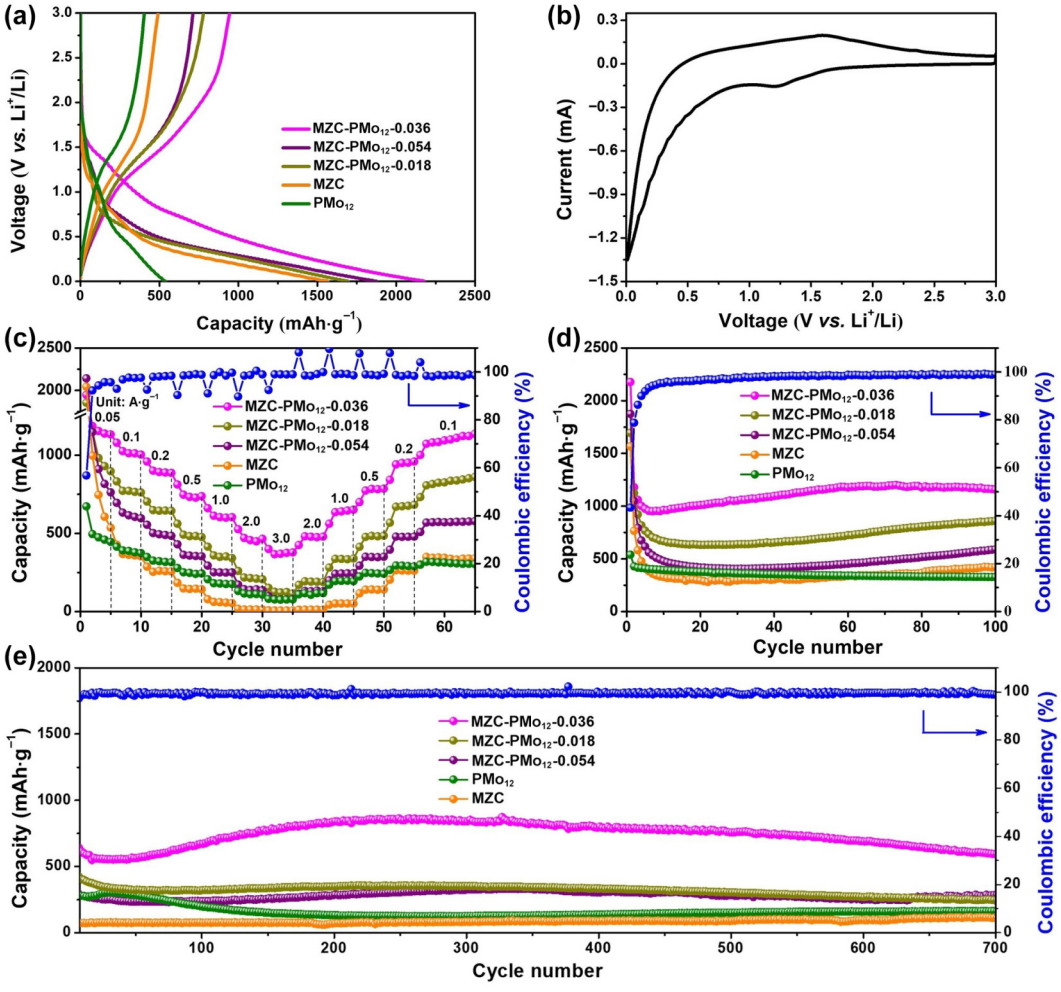

Figure 10 (a) Initial galvanostatic discharge–charge curves at 100 mA·g^{-1}. (b) CV profile of MnZnCuO$_x$-PMo$_{12}$-0.036 at 0.5 mV·s^{-1}. (c) Rate performance at various current densities. Long-term cycling tests at (d) 100 mA·g^{-1} and (e) 1.0 A·g^{-1}, with the blue lines representing the Coulombic efficiency of MnZnCuO$_x$-PMo$_{12}$-0.036 (PMA represents PMo$_{12}$ and MZC stands for MnZnCuO$_x$). Reproduced with permission from Ref. [56], © Wiley-VCH GmbH 2023.

4.3.2 *Na-ion batteries*

Nuclei-cluster coassemblies can also be used as anode materials for Na-ion batteries. Liu et al. used metal oxide-POM assemblies, including CeO$_x$-PMo$_{12}$, ZrCeO$_x$-PMo$_{12}$, FeZrCeO$_x$-PMo$_{12}$, NiFeZrCeO$_x$-PMo$_{12}$, CuNiFeZrCeO$_x$-PMo$_{12}$, ZnCuNiFeZrCeO$_x$-PMo$_{12}$, and CoZnCuNiFeZrCeO$_x$-PMo$_{12}$ sub-1 nm nanowires, as anode materials [46]. The initial Columbic efficiencies and capacity increased with the increasing number of metal oxides. CoZnCuNiFeZrCeO$_x$-PMo$_{12}$ nanowires delivered a reversible capacity of 305 mAh·g^{-1} at 0.1 C, exhibiting an outstanding rate performance and excellent cycling stability at 10 C. Moreover, this work represents the first report on the use of HEO-based materials as anode materials for Na-ion batteries.

4.3.3 *Li-O$_2$ batteries*

Ge et al. demonstrated that HEO-PMo$_{12}$ (BiCuFeCeWPtO$_x$-PMo$_{12}$) ultrathin nanowires act as cathode catalysts for Li-O$_2$ batteries, delivering a high capacity of 11,206 mAh·g^{-1} and outstanding cycling stability [60]. The capacity of Li-O$_2$ batteries increased with the increasing compositional complexity of the inorganic metal oxide nuclei (from binary to penternary). The incorporation of a sixth element (Ni, Mn, or Pt) into the penternary BiCuFeCeWO$_x$ system markedly affected capacity. Pt incorporation endowed the nanowire-based Li-O$_2$ battery with superior rate performance and enhanced cycling stability. This work offers a promising approach to the design and fabrication of efficient cathode catalysts for Li-O$_2$ batteries.

4.3.4 *Zn-air batteries*

As mentioned previously, CoFeNiMnCuZnO$_x$-PMo$_{12}$ SNSs are outstanding OER and ORR photoelectrocatalysts (Fig. 8(e)) [57] and can therefore serve as cathode materials when paired with a Zn foil anode to fabricate Zn-air batteries (Fig. 8(f)). Without illumination, the nanosheet-based Zn-air battery achieved a specific capacity (802 mAh·g^{-1}) markedly exceeding that (520 mAh·g^{-1}) of the battery with commercial catalysts (Pt/C with RuO$_2$) and exhibited a remarkable cycle life of 1600 h. Moreover, the nanosheet-based battery exhibited enhanced rechargeability under illumination, as evidenced by its higher discharge voltage and lower charge voltage.

4.3.5 *Li-S batteries*

Nuclei-cluster coassemblies can be utilized not only as anode materials but also as separators [67]. Owing to the polymer-like properties of sub-1 nm nanowires, Bi$_2$O$_3$-PMo$_{12}$ nanowires were

fabricated as highly flexible films (Fig. 11(a)) by injecting the nanowire dispersion into a mixture of octane and ethanol. These films were used as separators in Li-S batteries. The replacement of the traditional polypropylene (PP) separator by a Bi_2O_3-PMo_{12} film in an otherwise identical battery notably improved capacity and cycling stability (Fig. 11(b)), as the latter separator suppressed polysulfide shuttling and stabilized the Li anode. These results reveal that nuclei-cluster assemblies can act as not only anode materials but also as effective separators.

4.4 Other applications

Nuclei-POM coassemblies exhibit outstanding performance in the catalytic oxidation of organics, photo/electrocatalysis, and energy storage and show great potential for applications in other fields, such as solar steam generation, seawater desalination, and tumor treatment.

4.4.1 *Solar steam generation and seawater desalination*

MO_x-POM coassemblies can accelerate photothermal conversion because of their strong absorption in the ultraviolet and visible regions (Figs. 12(a) and 12(b)), thus holding promise for solar steam generation and seawater desalination. CuO-PMo_{12} nanosheets loaded on a cellulose acetate film were used for solar steam generation [50]. Under 1 sun illumination, the temperature around the film increased from 27 to ~ 53 °C in < 10 min (Fig. 12(c)). In the solar steam generation test, the CuO-PMo_{12} film, which floated on the surface of water, enhanced water evaporation (Fig. 12(d)) and thus accelerated solar steam generation. The CuO-PMo_{12} film was also used for seawater desalination (Fig. 12(e)), notably decreasing the concentration of primary ions (Fig. 12(f)). MoO_3-PMo_{12} nanobelts [52] and Bi_2O_3-PMo_{12} nanowires [54] also show great potential for solar steam generation and seawater desalination.

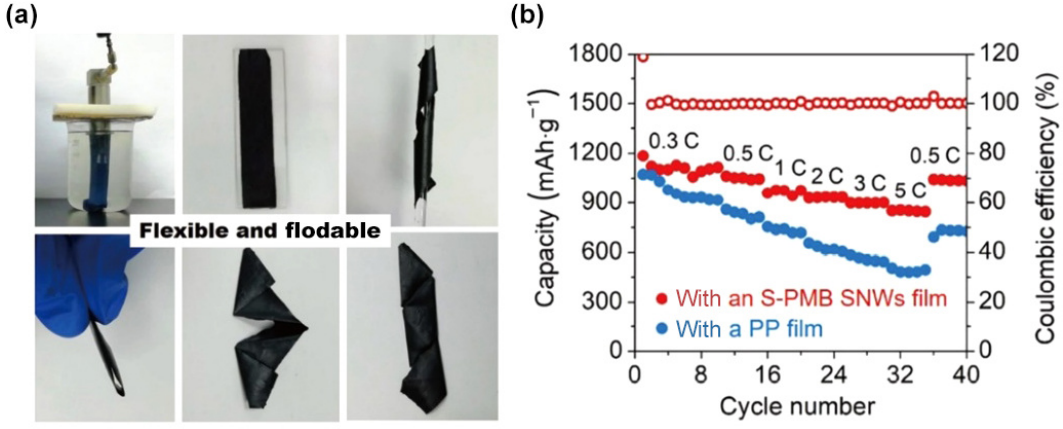

Figure 11 (a) The fabrication process of Bi_2O_3-PMo_{12} sub-1 nm nanowire films. The films could be further processed by twisting or folding. (b) Comparison of rate performance using a PP film and the super-aligned Bi_2O_3-PMo_{12} (S-PMB SNWs) film. Reproduced with permission from Ref. [67], © Science China Press and Springer-Verlag GmbH Germany, part of Springer Nature 2021.

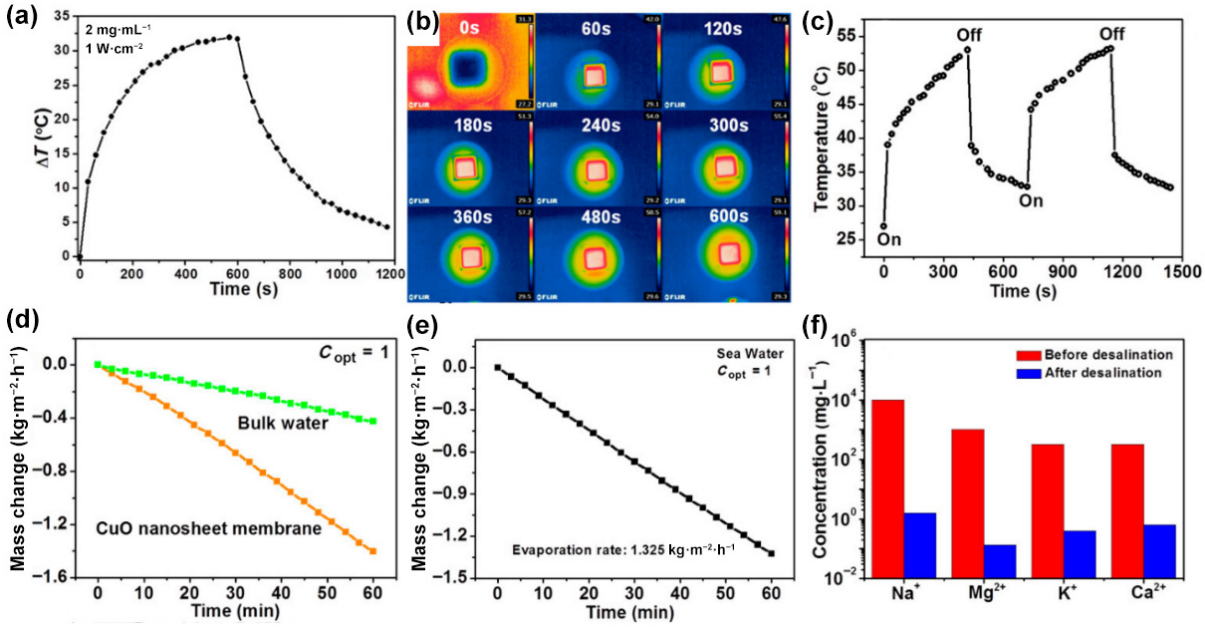

Figure 12 (a) The photothermal conversion efficiency of the CuO-PMo_{12} SNSs. (b) Photothermal images of the SNSs at different times, as monitored by an IR camera. (c) Photothermal cycling stability of the CuO-PMo_{12} film under 1 sun illumination. (d) Comparison of the mass change between bulk water and water covered with the CuO-PMo_{12} film under 1 sun illumination. (e) Evolution of seawater mass under 1 sun illumination with the CuO-PMo_{12} film. (f) Concentrations of major seawater ions pre- and post-desalination. Reproduced with permission from Ref. [50], © American Chemical Society 2019.

4.4.2 *Tumor treatment*

Tumor cells can be effectively killed by improving the yield of reactive oxygen species while depleting glutathione in the tumor microenvironment [86]. Wang et al. (2024) designed CoNi LDH-PMo_{12}-Au coassemblies and explored their applications in tumor treatment *in vitro* and *in vivo* [84]. The CoNi LDH-PMo_{12}-Au SNSs exhibited a stronger glutathione depletion activity than pure Au nanoparticles or CoNi LDH-PMo_{12}, which was attributed to the formation of sub-1 nm Au in the nanosheets. HeLa cells were selected as the research subject. When the cells were treated with ultrasound and CoNi LDH-PMo_{12}-Au, reactive oxygen species were generated. At the same time, once CoNi LDH-PMo_{12}-Au was added, remarkable glutathione depletion was observed. Therefore, tumor treatment was also carried out *in vivo* using a model established by injecting HeLa cells into mice. The combined effects of CoNi LDH-PMo_{12}-Au nanosheets and ultrasonication suppressed the growth of tumors and decreased their volume.

5 Conclusion and outlook

Diverse ultrathin nanomaterials showing outstanding performance in various applications have been developed using POM cluster-nuclei coassembly. The corresponding growth mechanism is thought to be applicable to all POM clusters and inorganic nuclei. Based on the diversity of POMs and inorganic nuclei, the near future will witness the emergence of more novel coassemblies with functional characteristics previously unattainable with individual components.

However, the study of cluster-nuclei coassembly is still in its infancy, and several key limitations must be addressed. First, current synthetic protocols often suffer from low yield, limited reproducibility, challenges in scale‐up, and moderate product stability. Second, the limited range of suitable POMs prevents the incorporation of many functional POM types. Thus, guiding principles should be established to predict POM structural characteristics suitable for cluster-nuclei coassembly. Third, the structures of coassembly products are largely unpredictable, which highlights the need for integrated methodologies that combine advanced MD simulations with experimental validation and thus enable structure prediction.

The application of high-throughput computational screening and machine learning methods is expected to enable the rapid exploration of diverse libraries of POMs and inorganic nuclei and thus lead to the discovery of novel cluster-nuclei coassemblies and optimized assembly conditions. If the above challenges can be overcome, POM-nuclei coassemblies will demonstrate considerable value across a wide range of fields. Moreover, POM-nuclei coassembled ultrathin materials hold promise for a wide range of applications, such as catalysis, energy storage and transfer, photothermal conversion, tumor treatment, and nanoelectronics.

Data availability

Not applicable.

Acknowledgements

This work was supported by the startup grant in Tianjin University of Technology.

Declaration of competing interest

The authors have no competing interests to declare that are relevant to the content of this article.

Author contribution statement

P. L. H.: Conceptualization, investigation, visualization, funding acquisition, writing manuscript.

Use of AI statement

None.

References

[1] Kagan, C. R.; Bassett, L. C.; Murray, C. B.; Thompson, S. M. Colloidal quantum dots as platforms for quantum information science. *Chem. Rev.* **2021**, *121*, 3186–3233.
[2] Brus, L. E. Electron-electron and electron-hole interactions in small semiconductor crystallites: The size dependence of the lowest excited electronic state. *J. Chem. Phys.* **1984**, *80*, 4403–4409.
[3] Nirmal, M.; Brus, L. Luminescence photophysics in semiconductor nanocrystals. *Acc. Chem. Res.* **1999**, *32*, 407–414.
[4] Murray, C. B.; Norris, D. J.; Bawendi, M. G. Synthesis and characterization of nearly monodisperse CdE (E = sulfur, selenium, tellurium) semiconductor nanocrystallites. *J. Am. Chem. Soc.* **1993**, *115*, 8706–8715.
[5] Bruchez, M.; Moronne, M.; Gin, P.; Weiss, S.; Alivisatos, A. P. Semiconductor nanocrystals as fluorescent biological labels. *Science* **1998**, *281*, 2013–2016.
[6] Michalet, X.; Pinaud, F. F.; Bentolila, L. A.; Tsay, J. M.; Doose, S.; Li, J. J.; Sundaresan, G.; Wu, A. M.; Gambhir, S. S.; Weiss, S. Quantum dots for live cells, *in vivo* imaging, and diagnostics. *Science* **2005**, *307*, 538–544.
[7] Bao, J.; Bawendi, M. G. A colloidal quantum dot spectrometer. *Nature* **2015**, *523*, 67–70.
[8] Pietryga, J. M.; Park, Y. S.; Lim, J.; Fidler, A. F.; Bae, W. K.; Brovelli, S.; Klimov, V. I. Spectroscopic and device aspects of nanocrystal quantum dots. *Chem. Rev.* **2016**, *116*, 10513–10622.
[9] Jin, R. C.; Zeng, C. J.; Zhou, M.; Chen, Y. X. Atomically precise colloidal metal nanoclusters and nanoparticles: Fundamentals and opportunities. *Chem. Rev.* **2016**, *116*, 10346–10413.
[10] Zhang, S. M.; Wang, X. Sub-1 nm: A critical feature size in materials science. *Acc. Mater. Res.* **2022**, *3*, 1285–1298.
[11] Cademartiri, L.; Ozin, G. A. Ultrathin nanowires-a materials chemistry perspective. *Adv. Mater.* **2009**, *21*, 1013–1020.
[12] Ni, B.; Shi, Y. A.; Wang, X. The sub-nanometer scale as a new focus in nanoscience. *Adv. Mater.* **2018**, *30*, 1802031.
[13] Hu, S.; Wang, X. Ultrathin nanostructures: Smaller size with new phenomena. *Chem. Soc. Rev.* **2013**, *42*, 5577–5594.
[14] Zhang, F. H.; Shi, W. X.; Liu, Q. D.; Wang, X. Modular assembly of polyoxometalate clusters at the sub-1 nm scale. *Nat. Protoc.* **2026**, *21*, 347–372.
[15] Ni, B.; Liu, H. L.; Wang, P. P.; He, J.; Wang, X. General synthesis of inorganic single-walled nanotubes. *Nat. Commun.* **2015**, *6*, 8756.
[16] Hu, S.; Liu, H. L.; Wang, P. P.; Wang, X. Inorganic nanostructures with sizes down to 1 nm: A macromolecule analogue. *J. Am. Chem. Soc.* **2013**, *135*, 11115–11124.
[17] Zhang, S. M.; Wang, X. Inorganic subnanometer nanowire-based organogels: Trends, challenges, and opportunities. *ACS Nano* **2023**, *17*, 20–26.
[18] Liu, H. L.; Gong, Q. H.; Yue, Y. H.; Guo, L.; Wang, X. Sub-1 nm nanowire based superlattice showing high strength and low modulus. *J. Am. Chem. Soc.* **2017**, *139*, 8579–8585.
[19] Zhang, S. M.; Lin, H. F.; Yang, H. Z.; Ni, B.; Li, H. Y.; Wang, X.

Highly flexible and stretchable nanowire superlattice fibers achieved by spring-like structure of sub-1 nm nanowires. *Adv. Funct. Mater.* **2019**, *29*, 1903477.
[20] Zhang, S. M.; Shi, W. X.; Rong, S. J.; Li, S. Z.; Zhuang, J.; Wang, X. Chirality evolution from sub-1 nanometer nanowires to the macroscopic helical structure. *J. Am. Chem. Soc.* **2020**, *142*, 1375–1381.
[21] Yang, Y.; Yang, Y.; Chen, S. M.; Lu, Q. C.; Song, L.; Wei, Y.; Wang, X. Atomic-level molybdenum oxide nanorings with full-spectrum absorption and photoresponsive properties. *Nat. Commun.* **2017**, *8*, 1559.
[22] Zhang, S. M.; Shi, Y. A.; He, T.; Ni, B.; Li, C. Z.; Wang, X. Ultrathin tungsten bronze nanowires with efficient photo-to-thermal conversion behavior. *Chem. Mater.* **2018**, *30*, 8727–8731.
[23] Yuan, F.; Ouyang, C.; Yang, M. Z.; Shi, W. X.; Ren, W. B.; Shen, Y.; Wei, Y.; Deng, X. L.; Wang, X. Regulating the mechanical and optical properties of polymer-based nanocomposites by sub-nanowires. *Angew. Chem., Int. Ed.* **2023**, *62*, e202214571.
[24] Yu, B.; Xiu, Y. Y.; Zhang, S. M.; Wang, X. Polymer-like photochromic tungsten oxide sub-1 nm nanowires. *J. Am. Chem. Soc.* **2025**, *147*, 26626–26634.
[25] Zhang, S. M.; Shi, W. X.; Wang, X. Locking volatile organic molecules by subnanometer inorganic nanowire-based organogels. *Science* **2022**, *377*, 100–104.
[26] Liu, J. L.; Shi, W. X.; Ni, B.; Yang, Y.; Li, S. Z.; Zhuang, J.; Wang, X. Incorporation of clusters within inorganic materials through their addition during nucleation steps. *Nat. Chem.* **2019**, *11*, 839–845.
[27] Cheng, X. J.; Zhang, S. M.; Wang, X. Cluster-nuclei coassembled one-dimensional subnanometer heteronanostructures. *Nano Lett.* **2021**, *21*, 9845–9852.
[28] Wang, S. S.; Yang, G. Y. Recent advances in polyoxometalate-catalyzed reactions. *Chem. Rev.* **2015**, *115*, 4893–4962.
[29] Cai, Q. M.; Gao, R. L.; Wang, Y. F.; Xing, J. S.; Zhang, Q. Y.; Zhu, M. Z.; Qin, X. Y.; Liao, M. H.; Huang, Y. C. Ruthenium containing polyoxometalates: From synthesis, structures, properties to functional applications. *Polyoxometalates* **2025**, *4*, 9140083.
[30] Lian, X. K.; Chen, H. B.; Lin, Y. D.; Li, X. X.; Zheng, S. T. Polyoxometalate-based all-inorganic open frameworks. *Coord. Chem. Rev.* **2023**, *497*, 215440.
[31] Long, D. L.; Burkholder, E.; Cronin, L. Polyoxometalate clusters, nanostructures and materials: From self assembly to designer materials and devices. *Chem. Soc. Rev.* **2007**, *36*, 105–121.
[32] Liu, Q. D.; Zhang, Q. H.; Shi, W. X.; Hu, H. S.; Zhuang, J.; Wang, X. Self-assembly of polyoxometalate clusters into two-dimensional clusterphene structures featuring hexagonal pores. *Nat. Chem.* **2022**, *14*, 433–440.
[33] Fan, D. W.; Jia, X. F.; Tang, P. Q.; Hao, J. C.; Liu, T. B. Self-patterning of hydrophobic materials into highly ordered honeycomb nanostructures at the air/water interface. *Angew. Chem., Int. Ed.* **2007**, *46*, 3342–3345.
[34] Bu, W. F.; Li, H. L.; Sun, H.; Yin, S. Y.; Wu, L. X. Polyoxometalate-based vesicle and its honeycomb architectures on solid surfaces. *J. Am. Chem. Soc.* **2005**, *127*, 8016–8017.
[35] Nisar, A.; Xu, X. X.; Shen, S. L.; Hu, S.; Wang, X. Noble metal nanocrystal-incorporated fullerene-like polyoxometalate based microspheres. *Adv. Funct. Mater.* **2009**, *19*, 860–865.
[36] He, P. L.; Xu, B.; Wang, P. P.; Liu, H. L.; Wang, X. A monolayer polyoxometalate superlattice. *Adv. Mater.* **2014**, *26*, 4339–4344.
[37] Proust, A.; Thouvenot, R.; Gouzerh, P. Functionalization of polyoxometalates: Towards advanced applications in catalysis and materials science. *Chem. Commun.* **2008**, 1837–1852.
[38] Zhu, H. X.; Liu, Y.; Wu, A. P.; Wang, D. X.; Fan, Y. Y.; Yue, X. Y.; Jiao, Y. Q.; Lian, Y. F.; Tian, C. G. Nanosheet-based 3-dimentional assembly with synergitic Co–Mo sites for effective electrocatalytic hydrogen evolution reaction. *Chem. Eng. J.* **2025**, *510*, 161490.
[39] LaMer, V. K.; Dinegar, R. H. Theory, production and mechanism of formation of monodispersed hydrosols. *J. Am. Chem. Soc.* **1950**, *72*, 4847–4854.
[40] Vreeland, E. C.; Watt, J.; Schober, G. B.; Hance, B. G.; Austin, M. J.; Price, A. D.; Fellows, B. D.; Monson, T. C.; Hudak, N. S.; Maldonado-Camargo, L. et al. Enhanced nanoparticle size control by extending LaMer's mechanism. *Chem. Mater.* **2015**, *27*, 6059–6066.
[41] Li, J. J.; Deepak, F. L. *In situ* kinetic observations on crystal nucleation and growth. *Chem. Rev.* **2022**, *122*, 16911–16982.
[42] Kwon, H. J.; Shin, K.; Soh, M.; Chang, H.; Kim, J.; Lee, J.; Ko, G.; Kim, B. H.; Kim, D.; Hyeon, T. Large-scale synthesis and medical applications of uniform-sized metal oxide nanoparticles. *Adv. Mater.* **2018**, *30*, 1704290.
[43] Liu, Q. D.; Wang, X. Y.; Wang, X. Sub-1 nm materials chemistry: Challenges and prospects. *J. Am. Chem. Soc.* **2024**, *146*, 26587–26602.
[44] Liu, J. L.; Wang, S. B.; Liu, N.; Yang, D. R.; Wang, H. W.; Hu, H. S.; Zhuang, J.; Wang, X. Au-polyoxometalates A-B-A-B type copolymer ‐ analogue sub-1 nm nanowires. *Small* **2021**, *17*, 2006260.
[45] Boulicault, J. E.; Alves, S.; Cole, R. B. Negative Ion MALDI mass spectrometry of polyoxometalates (POMs): Mechanism of singly charged anion formation and chemical properties evaluation. *J. Am. Soc. Mass Spectrom.* **2016**, *27*, 1301–1313.
[46] Liu, J. L.; Li, Y. Q.; Chen, Z.; Liu, N.; Zheng, L. R.; Shi, W. X.; Wang, X. Polyoxometalate cluster-incorporated high entropy oxide sub-1 nm nanowires. *J. Am. Chem. Soc.* **2022**, *144*, 23191–23197.
[47] Akram, B.; Shi, W. X.; Zhang, H.; Ullah, S.; Khurram, M.; Wang, X. Free-standing CoO-POM Janus-like ultrathin nanosheets. *Angew. Chem.* **2020**, *132*, 8575–8579.
[48] Yang, H. Z.; Yang, D. R.; Wang, X. POM-incorporated CoO nanowires for enhanced photocatalytic syngas production from CO_2. *Angew. Chem., Int. Ed.* **2020**, *59*, 15527–15531.
[49] Liu, J. L.; Shi, W. X.; Wang, X. ZnO-POM cluster sub-1 nm nanosheets as robust catalysts for the oxidation of thioethers at room temperature. *J. Am. Chem. Soc.* **2021**, *143*, 16217–16225.
[50] Liu, J. L.; Shi, W. X.; Wang, X. Cluster-nuclei coassembled into two-dimensional hybrid CuO-PMA sub-1 nm nanosheets. *J. Am. Chem. Soc.* **2019**, *141*, 18754–18758.
[51] Zhang, S. M.; Liu, N.; Wang, H. W.; Lu, Q. C.; Shi, W. X.; Wang, X. Sub ‐ nanometer nanobelts based on titanium dioxide/zirconium dioxide-polyoxometalate heterostructures. *Adv. Mater.* **2021**, *33*, 2100576.
[52] Liu, J. L.; Liu, N.; Wang, H. W.; Shi, W. X.; Zhuang, J.; Wang, X. Hybrid MoO_3-polyoxometallate sub-1 nm nanobelt superstructures. *J. Am. Chem. Soc.* **2020**, *142*, 17557–17563.
[53] Liu, J. L.; Shi, W. X.; Nie, S. Y.; Wang, X. Functionally guided precise synthesis of manganous oxide-polyoxometalate 2D hybrid sub-1 nm nanosheet superstructures. *Small Struct.* **2022**, *3*, 2200039.
[54] Zhang, S. M.; Lu, Q. C.; Yu, B.; Cheng, X. J.; Zhuang, J.; Wang, X. Polyoxometalates facilitating synthesis of subnanometer nanowires. *Adv. Funct. Mater.* **2021**, *31*, 2100703.
[55] Nie, S. Y.; Wu, L.; Wang, X. Electron-delocalization-stabilized photoelectrocatalytic coupling of methane by NiO-polyoxometalate sub-1 nm heterostructures. *J. Am. Chem. Soc.* **2023**, *145*, 23681–23690.
[56] Yuan, G. B.; Ge, H. Y.; Shi, W. X.; Liu, J. L.; Zhang, Y.; Wang, X. Hybrid sub-1 nm nanosheets of co-assembled $MnZnCuO_x$ and polyoxometalate clusters as anodes for Li-ion batteries. *Angew. Chem., Int. Ed.* **2023**, *62*, e202309934.
[57] Ge, H. Y.; Zheng, L. R.; Yuan, G. B.; Shi, W. X.; Liu, J. L.; Zhang, Y.; Wang, X. Polyoxometallate cluster Induced high-entropy oxide sub-1 nm nanosheets as photoelectrocatalysts for Zn-air batteries. *J. Am. Chem. Soc.* **2024**, *146*, 10735–10744.
[58] Cheng, X. J.; Nie, S. Y.; Huang, Y.; Liu, Q. D.; Wu, L.; Wang, X. Electron-delocalization across high surface entropy sub-1 nm nanobelts toward enhanced electrocatalytic urea oxidation. *Small* **2024**, *20*, 2404595.
[59] Cao, X. J.; Zhai, J. X.; Zhao, Y. L.; Rui, K.; Shi, W. X.; Zhao, H. B.; He, P. L. Sub‐1 nm high-entropy oxide nanosheets for robust oxygen

evolution reaction at large current density. *Sci. China Chem.* **2026**, *69*, 190–196.
[60] Ge, H. Y.; Shi, W. X.; Liu, J. L.; Zhang, Y.; Wang, X. High entropy oxide-polyoxometalate sub-1 nm hetero-nanowires as cathode catalysts in Li–O_2 batteries. *J. Am. Chem. Soc.* **2025**, *147*, 8367–8376.
[61] Liu, J. L.; Zhuang, J.; Shi, W. X.; Wang, X. $Ni(OH)_2$-polyoxometalate cluster hybrid superstructures. *Chem. Mater.* **2021**, *33*, 7100–7105.
[62] Wang, Z. R.; Ye, Q. H.; Chen, W. C.; Zhao, Y. L.; Cao, X. J.; Shi, W. X.; He, P. L. Electronic structure engineering of sub-1 nm $Ni(OH)_2$ nanowires through Fe incorporation in polyoxometalates for superior water oxidation. *Adv. Funct. Mater.* **2026**, *36*, e11187.
[63] Yang, D. R.; Zuo, S. W.; Yang, H. Z.; Wang, X. Single-unit-cell catalysis of CO_2 electroreduction over sub-1 nm Cu_9S_5 nanowires. *Adv. Energy Mater.* **2021**, *11*, 2100272.
[64] Cai, M. X.; Ye, Q. H.; Wang, Z. R.; He, P. L. Sub-1 nm Ni_3S_2–$FeMo_6$ nanosheets through cluster-nuclei coassembled strategy for high-efficiency water oxidation. *Int. J. Hydrogen Energy* **2025**, *170*, 151258.
[65] Liu, Q. D.; He, S. Q.; Yu, B.; Cheng, X. J.; Shi, W. X.; Wang, X. Visible light induced Ag-polyoxometalate coassembly into single-cluster nanowires. *Adv. Mater.* **2022**, *34*, 2206178.
[66] Akram, B.; Ni, B.; Wang, X. van der Waals integrated hybrid POM-zirconia flexible belt-like superstructures. *Adv. Mater.* **2020**, *32*, 1906794.
[67] Zhang, S. M.; Shi, H. D.; Tang, J. W.; Shi, W. X.; Wu, Z. S.; Wang, X. Super-aligned films of sub-1 nm Bi_2O_3-polyoxometalate nanowires as interlayers in lithium-sulfur batteries. *Sci. China Mater.* **2021**, *64*, 2949–2957.
[68] Sarkar, A.; Wang, Q. S.; Schiele, A.; Chellali, M. R.; Bhattacharya, S. S.; Wang, D.; Brezesinski, T.; Hahn, H.; Velasco, L.; Breitung, B. High-entropy oxides: Fundamental aspects and electrochemical properties. *Adv. Mater.* **2019**, *31*, 1806236.
[69] Aamlid, S. S.; Oudah, M.; Rottler, J.; Hallas, A. M. Understanding the role of entropy in high entropy oxides. *J. Am. Chem. Soc.* **2023**, *145*, 5991–6006.
[70] Gao, D. D.; Zhu, W. X.; Chen, J. X.; Qin, K. Y.; Ma, M. J.; Shi, J.; Wang, Q.; Fan, Z. L.; Shao, Q.; Liao, F. et al. High-entropy effect promoting self-healing behavior of two-dimensional metal oxide electrocatalysts for oxygen evolution reaction. *ACS Catal.* **2024**, *14*, 3700–3711.
[71] Baek, J.; Hossain, M. D.; Mukherjee, P.; Lee, J.; Winther, K. T.; Leem, J.; Jiang, Y.; Chueh, W. C.; Bajdich, M.; Zheng, X. L. Synergistic effects of mixing and strain in high entropy spinel oxides for oxygen evolution reaction. *Nat. Commun.* **2023**, *14*, 5936.
[72] Nie, S. Y.; Wu, L.; Zhang, Q. H.; Huang, Y. W.; Liu, Q. D.; Wang, X. High-entropy-perovskite subnanowires for photoelectrocatalytic coupling of methane to acetic acid. *Nat. Commun.* **2024**, *15*, 6669.
[73] Qian, D. Q.; Lin, Y. D.; Xiao, H. P.; Wu, B.; Li, X. X.; Zheng, S. T. Advances in coinage-metal-substituted polyoxometalates: A review. *Polyoxometalates* **2024**, *3*, 9140040.
[74] Zheng, S. T.; Yang, G. Y. Recent advances in paramagnetic-TM-substituted polyoxometalates (TM = Mn, Fe, Co, Ni, Cu). *Chem. Soc. Rev.* **2012**, *41*, 7623–7646.
[75] Izarova, N. V.; Banerjee, A.; Kortz, U. Noble metals in polyoxometalate chemistry: Palladium-containing derivatives of the monolacunary Keggin and Wells-Dawson tungstophosphates. *Inorg. Chem.* **2011**, *50*, 10379–10386.
[76] Cao, R.; Ma, H. Y.; Geletii, Y. V.; Hardcastle, K. I.; Hill, C. L. Structurally characterized Iridium(III)-containing polytungstate and catalytic water oxidation activity. *Inorg. Chem.* **2009**, *48*, 5596–5598.
[77] Blasco-Ahicart, M.; Soriano-López, J.; Carbó, J. J.; Poblet, J. M.; Galan-Mascaros, J. R. Polyoxometalate electrocatalysts based on earth-abundant metals for efficient water oxidation in acidic media. *Nat. Chem.* **2018**, *10*, 24–30.
[78] Yang, T. H.; Ahn, J.; Shi, S.; Wang, P.; Gao, R. Q.; Qin, D. Noble-metal nanoframes and their catalytic applications. *Chem. Rev.* **2021**, *121*, 796–833.
[79] Hartland, G. V. Optical studies of dynamics in noble metal nanostructures. *Chem. Rev.* **2011**, *111*, 3858–3887.
[80] Chen, H. J.; Shao, L.; Li, Q.; Wang, J. F. Gold nanorods and their plasmonic properties. *Chem. Soc. Rev.* **2013**, *42*, 2679–2724.
[81] Li, J.; Li, X.; Zhai, H. J.; Wang, L. S. Au_{20}: A tetrahedral cluster. *Science* **2003**, *299*, 864–867.
[82] Petrova, H.; Lin, C. H.; Hu, M.; Chen, J. Y.; Siekkinen, A. R.; Xia, Y. N.; Sader, J. E.; Hartland, G. V. Vibrational response of Au−Ag nanoboxes and nanocages to ultrafast laser-induced heating. *Nano Lett.* **2007**, *7*, 1059–1063.
[83] Xiong, Y. J.; Chen, J. Y.; Wiley, B.; Xia, Y. N.; Yin, Y. D.; Li, Z. Y. Size-dependence of surface plasmon resonance and oxidation for Pd nanocubes synthesized via a seed etching process. *Nano Lett.* **2005**, *5*, 1237–1242.
[84] Wang, D.; Yuan, F.; Deng, X. L.; Liu, Q. D.; Shi, W. X.; Wang, X. Sub-nanosheet induced inverse growth of negative valency Au clusters for tumor treatment by enhanced oxidative stress. *Angew. Chem., Int. Ed.* **2024**, *63*, e202410649.
[85] Liu, J. L.; Wang, M. X.; Dipalo, M. C.; Zhuang, J.; Shi, W. X.; Wang, X. Ternary hybrid CuO-PMA-Ag sub-1 nm nanosheet heterostructures. *Chem. Sci.* **2021**, *12*, 11490–11494.
[86] Ma, X. Q.; Cai, D.; Zhang, Z. X.; Dai, Q.; Li, X. Y.; Yu, B.; Ge, B. S.; Liu, S. H.; Wang, X. J.; Huang, F. Peptidomimetic-liganded gold nanoclusters for controlled iron delivery and synergistic suppression of tumor growth. *Nano Res.* **2023**, *16*, 12066–12075.

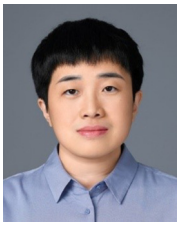

Peilei He is a professor in Tianjin University of Technology since 2025. She received her Ph.D. degree from the Department of Chemistry, Tsinghua University in 2016. Then she worked as a research fellow at Nanyang Technological University, Singapore. Starting from 2018, she worked as a postdoc at Marquette University and Iowa State University in United States. From 2021 to 2025, she worked as a professor at Ningbo Institute of Materials Technology and Engineering, CAS. In 2025, she joined School of Materials Science and Engineering, Tianjin University of Technology as full professor. Her research interests mainly focus on synthesis and self-assembly of sub-nano/nano structures for energy-related catalysis.